The bulk van der Waals layered magnet CrSBr is a quasi-1D quantum material

J. Klein,[1,*] B. Pingault,[2,3] M. Florian,[4] M.C. Heißenbüttel,[5] A. Steinhoff,[6,7] Z. Song,[2] K. Torres,[1] F. Dirnberger,[8] J.B. Curtis,[2] T. Deilmann,[5] R. Dana,[1] R. Bushati,[8,9] J. Quan,[10,11,12,13] J. Luxa,[14] Z. Sofer,[14] A. Alù,[10,11,12,13] V. M. Menon,[8,9] U. Wurstbauer,[15] M. Rohlfing,[5] P. Narang,[2,†] M. Lončar,[2,‡] and F. M. Ross[1,§]

[1] *Department of Materials Science and Engineering, Massachusetts Institute of Technology, Cambridge, Massachusetts 02139, USA*
[2] *John A. Paulson School of Engineering and Applied Sciences, Harvard University, Cambridge, MA, USA*
[3] *QuTech, Delft University of Technology, 2600 GA Delft, The Netherlands*
[4] *Department of Electrical and Computer Engineering, Department of Physics, University of Michigan, Ann Arbor, Michigan 48109, United States*
[5] *Institut für Festkörpertheorie, Westfälische Wilhelms-Universität Münster, 48149 Münster, Germany*
[6] *Institut für Theoretische Physik, Universität Bremen, P.O. Box 330 440, 28334 Bremen, Germany*
[7] *Bremen Center for Computational Materials Science, University of Bremen, 28359, Bremen, Germany*
[8] *Department of Physics, City College of New York, New York, NY 10031, USA*
[9] *Department of Physics, The Graduate Center, City University of New York, New York, NY 10016, USA*
[10] *Department of Electrical and Computer Engineering, The University of Texas at Austin, Austin, TX, 78712, USA*
[11] *Photonics Initiative, CUNY Advanced Science Research Center, New York, NY, 10031, USA*
[12] *Department of Electrical Engineering, City College of the City University of New York, New York, NY, 10031, USA*
[13] *Physics Program, Graduate Center, City University of New York, New York, NY, 10026, USA*
[14] *Department of Inorganic Chemistry, University of Chemistry and Technology Prague, Technická 5, 166 28 Prague 6, Czech Republic*
[15] *Institute of Physics and Center for Nanotechnology, University of Münster, 48149 Münster, Germany*

(Dated: 2022-05-27)

Correlated quantum phenomena in one-dimensional (1D) systems that exhibit competing electronic and magnetic orders are of fundamental interest. Interaction effects in low-dimensional systems can lead to fundamental excitations which are completely different from the quasi-particles one would expect in a higher-dimensional counterpart, such as Tomonaga-Luttinger liquids and topological orders and defects. However, clean 1D electronic systems are difficult to realize experimentally, particularly magnetically ordered systems. Here, we show that the van der Waals layered magnetic semiconductor CrSBr behaves like a quasi-1D electronic material embedded in a magnetically ordered environment. The strong 1D electronic character is due to the unique combination of weak interlayer hybridization and anisotropy in effective mass and dielectric screening. The band structure and quasi-particle excitations are dominated by the Cr-S chains and a shallow 1D quantum confinement normal to these chains, manifesting in an anisotropic band with an effective electron mass ratio of $m_X^e/m_Y^e \sim 50$. Strong quasi-particle interactions and 1D electronic character are indicated by Fano resonances from a van Hove singularity of similar strength as in metallic carbon nanotubes. The spectrally narrow excitons (1 meV) inherit the 1D character and show pronounced exciton-phonon coupling effects. Overall, CrSBr appears to be an experimentally clean candidate for the study of 1D correlated many-body physics in the presence of magnetic order.

Experimental realizations of one-dimensional platforms for studying quantum phenomena are rare, some examples being ultra-cold quantum gases, [1] atomic chains [2] or carbon nanotubes. [3–8] While such platforms are essential for the study of correlated phenomena like Tomonaga-Luttinger liquids, [2, 5] 1D spin chains [9] or for realizing quantum conducting wires, [10] they may be unstable, hard to scale up or suffer from ensemble inhomogeneities.

Quasi-1D electronic systems are an appealing alternative. Examples include MoS_2 [11] and hBN nanotubes, [12] III-V-based nanowires [13, 14] or other quasi-1D materials like $ZrTe_3$, [15] $NbSe_3$ [16] or $TiSe_3$. [17] Some systems show interesting quantum phenomena such as charge density wave physics (CDW) [15]. Low-dimensional systems with both electronic and magnetic character are particularly intriguing and several efforts have been dedicated to their design and fabrication. [18] Early examples include dilute magnetic semiconductors like Mn-doped quantum wells and quantum wires that exhibit electronic and optical excitations that are strongly correlated with the magnetic degree of freedom. [19, 20]

A particularly exciting development is the observation of long-range magnetic order in van der Waals magnets. [21, 22] Such materials attract interest due to their correlated excitations including electron-electron, electron-spin, exchange and electron-phonon interactions that are expected to result in new exotic quantum phenomena and functionalities. This motivates the exploration of new quantum materials that are low-

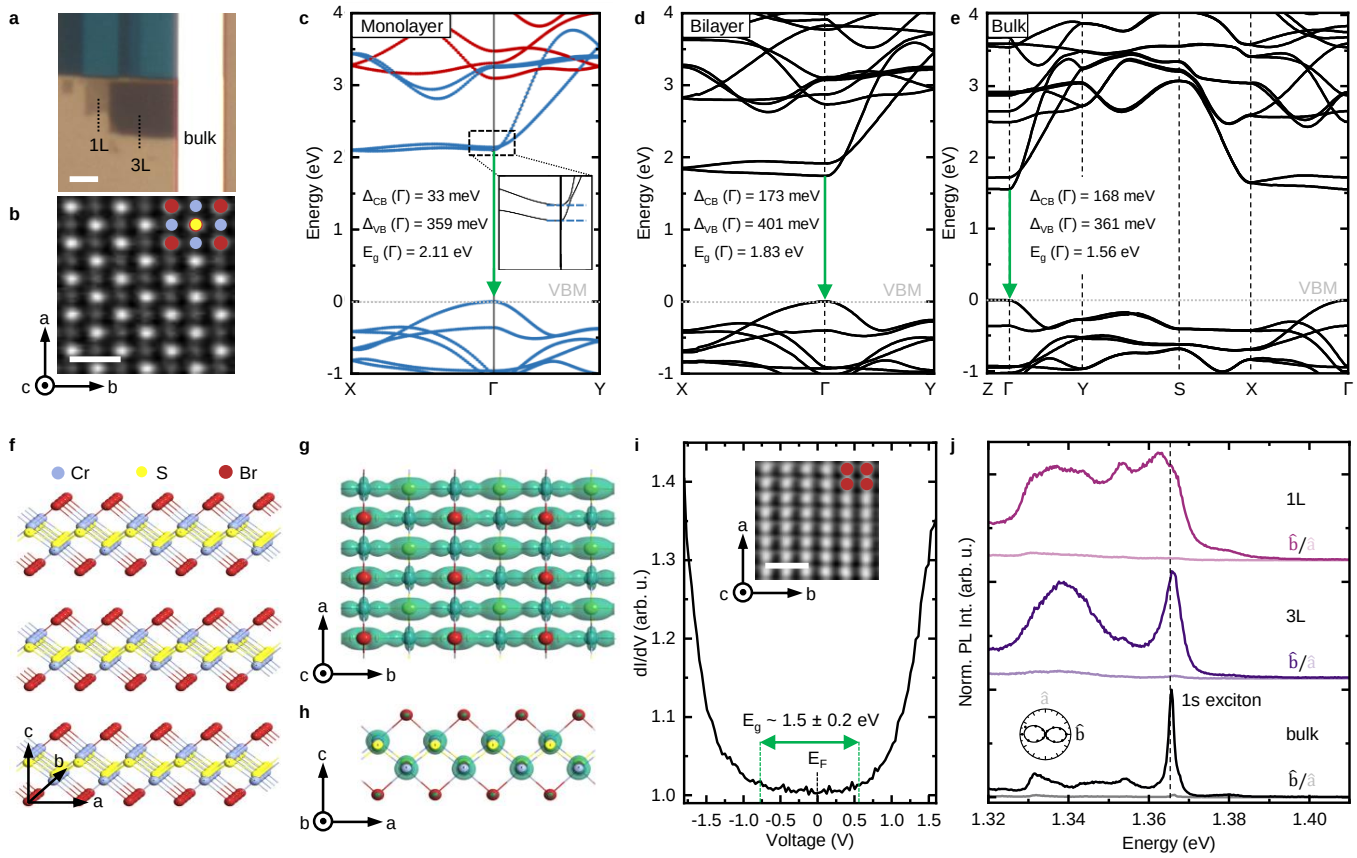

FIG.| 1. **Quasi-1D electronic structure of CrSBr in the bulk.** **a**, Optical micro-graph of mechanically exfoliated CrSBr. Needle-like crystals extend along the a-direction. Scale bar is 4 µm. **b**, STEM-HAADF image of multilayer CrSBr taken at an electron beam energy of 200 keV. Scale bar is 0.5 nm. **c**, 1L CrSBr DFT-GW calculation of the high symmetry points $X-\Gamma-Y$ showing a flat conduction band along the $\Gamma-X$ direction (effective electron mass $m_X^e = 7.31m_0$) and a highly dispersive band along the $\Gamma-Y$ direction ($m_Y^e = 0.14m_0$). The blue and red colors represent the majority and minority (in-plane) spin polarization. Inset: Zoom in of the split conduction bands at Γ ($\Delta_{\mathrm{CB}} = 33$ meV). **d**, and **e** show DFT-GW calculations of the 2L and bulk CrSBr. **f-h**, Schematic illustration of bulk CrSBr with the relevant electronic structure that is formed by atomic orbitals mainly from the Cr and S orbitals. The charge density of states near the Fermi level is shown as obtained by DFT calculations. The charge density includes the states in the range 0.1 eV below the top of the valence band and 0.1 eV above the bottom of the conduction band. Although the atomic distance in the a-direction is less than in the b-direction, the electronic states form chains (charge density in green) along the b-direction that are only weakly hybridized (coupled) along the a-direction. **i**, Room temperature constant height dI/dV from STS ($I_t = 50$ pA at $V_{bias} = 0.2$ V) with a single-particle gap of $\sim 1.5 \pm 0.2$eV. Inset: Topographic STM image of CrSBr surface showing the Br atoms on the surface. Scale bar is 1 nm. **j**, Low-temperature (4.2 K) PL of 1L, 3L and bulk (36.8 nm $\sim$ 46L) CrSBr for the electric field co-polarized in excitation and detection along the b-and a-direction, respectively. The PL emission of the 1s exciton in bulk CrSBr is highlighted. Inset: Anisotropic 1s exciton emission of bulk CrSBr.

dimensional in nature, not only magnetically but also electronically.

A material that fulfills many requirements is the emergent van der Waals magnet CrSBr [23–27] from the group of chalcogen-halides that are described by the stoichiometric formula MXP. These consist of a transition metal (M = Cr, Fe, V), a chalcogen (X = S, Se, O) and a halogen (P = Br, Cl, I). Without including spin, the chalcogen-halides have space group 59 (Pmmn) and point group D_{2h}. CrSBr combines several particularly interesting properties. [23–33] It is a semiconductor with an energy gap of $\sim$ 1.5 eV. [25, 27] It is also an A-type antiferromagnet (AFM) with the magnetic easy-axis along the b-direction and a high Néel temperature of $T_N \sim 132$ K. [24, 27] A number of recent works have shown structural phase transformations, [31] magneto-optical [29] and magneto-transport [27, 32, 33] properties and exciton-magnon coupling. [34]

Understanding the underlying electronic structure, the quasi-particles and their mutual couplings is key to engineering magnetic properties in CrSBr. In another chalcogen-halide, TiOCl, Spin-Peierls and CDW physics

has been reported, [35–37] suggesting that materials with even larger structural anisotropy, such as CrSBr, may potentially show electronic 1D character. Indeed, a recent transport study has reported an unusual anisotropy in the electron conductivity along the a- and b- directions of CrSBr with striking ratios of up to 10^5, attributed to quasi-1D transport. [33] This observation motivates our interest in the origin of the peculiar electronic structure of CrSBr and its impact on the material's vibrational, optical and magnetic properties.

In this manuscript, we report evidence for quasi-1D electronic behavior of CrSBr based on both experiment and theory. We suggest that the strong 1D electronic character is due to a unique combination of weak interlayer hybridization and anisotropy in effective mass and dielectric screening that show unambiguously in all our experiments and calculations. Experimentally, the 1D electronic character manifests in strong exciton-phonon and electron-phonon interactions. By inelastic light scattering, we reveal a Breit-Wigner-Fano resonance in the phonon mode from resonant quasi-1D electron-phonon coupling effects with its origin in a 1D density of states (DOS). The 1D electronic character in combination with the absence of sample inhomogeneity from strain or substrate/surface effects that are very common in atomically thin materials results in clean optical signatures with spectrally narrow (1 meV) exciton emission in low-temperature photoluminescence (PL) measurements. The excitons inherit the 1D electronic character owing to the dominant orbital admixture from electronic flat bands and a quasi-1D dielectric screening. The low-dimensionality of bulk CrSBr is further corroborated by pronounced exciton-phonon interaction effects with the observation of exciton-phonon bound states from photoluminescence excitation (PLE) spectroscopy. Our work establishes bulk CrSBr as an ideal platform to explore rich quasi-particle excitations and their mutual couplings in a magnetically ordered environment.

Quasi-1D electronic structure of CrSBr. Unlike the previously investigated archetypal magnets CrI_3 and $Cr_2Ge_2Te_6$, [21, 22] CrSBr shows good air-stability and can be easily cleaved down to a monolayer (1L) (see Fig. 1a). Exfoliated crystals have a needle-like shape and exhibit a structural anisotropy (see Fig. 1b). [31] The strong electronic anisotropy is directly apparent from our 1L, 2L and bulk density functional theory (DFT-GW) calculation (see Fig. 1c-e). The 1L shows two conduction bands (energy splitting of 33 meV at the Γ point) that are flat along the a-direction ($\Gamma - X$) and highly dispersive along the b-direction ($\Gamma - Y$). The relevant electronic structure around the Γ-point can also be well described in a simple three-band $k \cdot p$ model (see SI). The Γ-point effective masses of the lowest conduction band and the topmost valence band in $\Gamma - X$- and $\Gamma - Y$-directions, respectively, are extracted from the DFT+GW band structures: $m_X^e = 7.31m_0$, $m_Y^e = 0.14m_0$, $m_X^h = 2.84m_0$, $m_Y^h = 0.45m_0$. This manifests in a pronounced effective electron mass anisotropy of $\frac{m_X^e}{m_Y^e} \sim 50$. This mass anisotropy is significantly higher as compared to anisotropic black phosphorous [38] The electronic anisotropy originates from the orbital composition of the electronic bands around the conduction band minimum (CBM) and the valence band maximum (VBM). This is best visualized by the charge density around the Fermi level of CrSBr with predominant admixture from the Cr-S chains along the b-direction (see Fig. 1g and h). The orbitals of the Br atoms only weakly admix into the conduction bands, resulting in the weakened interlayer hybridization. In the case of the 1L, we obtain admixtures to the lower conduction band of 64% Cr, 32% S and 4% Br and for the upper conduction band 86% Cr, 9% S and 5% Br. It is the dominant admixture of the Cr and S orbitals in the band structure that cause CrSBr's strong 1D electronic character, with a shallow 1D quantum confinement along the a-direction due to a weak intra-layer hybridization (coupling) of the chains. This weak hybridization is also apparent from the DFT-GW calculation of bilayer (2L) and bulk CrSBr (see Fig. 1d and e) and differs from semiconducting TMDCs. [39, 40] We obtain a qualitatively similar band structure for 1L, 2L and bulk along the $X - \Gamma - Y$ direction, as expected from the weak interlayer hybridization. The fundamental band gap is direct and situated at the Γ point, in addition to a nearly degenerate conduction band state at the X-point for the 1L. In general, we find that the effect of the flat band along $\Gamma - X$ becomes even more pronounced in the GW calculation. Moreover, the strong mass anisotropy results in a large density of states (DOS) along the $\Gamma - X$ direction at the band edge which is expected to be accompanied by a van Hove singularity (see SI).

In order to access the electronic states experimentally, we perform scanning tunneling microscopy (STM) and spectroscopy (STS) at room temperature ($T = 300$ K) on bulk CrSBr crystals cleaved under ultra high vacuum to obtain a clean surface. Figure 1i shows a typical dI/dV trace. The extracted size of the band gap, $E_g = 1.5 \pm 0.2$eV, is consistent with the bulk DFT-GW calculation yielding an energy gap of 1.56 eV (see Fig. 1e) and in agreement with a previous STS study. [27]

Low-temperature (4.2 K) PL (see Fig. 1j) confirms the weak interlayer hybridization of CrSBr, in line with all other findings. The optical emission of CrSBr is strongly linearly polarized along the b-direction reflecting the electronic anisotropy. The spectra from 1L, 3L and bulk (36.8 nm $\sim$ 46L) show a clear signature of the 1s exciton recombination at $\sim$ 1.366 eV along with other hitherto unidentified peaks energetically below the 1s exciton. Most importantly, the features in all spectra remain the same upon layer number reduction, but display significant line broadening that likely originates from

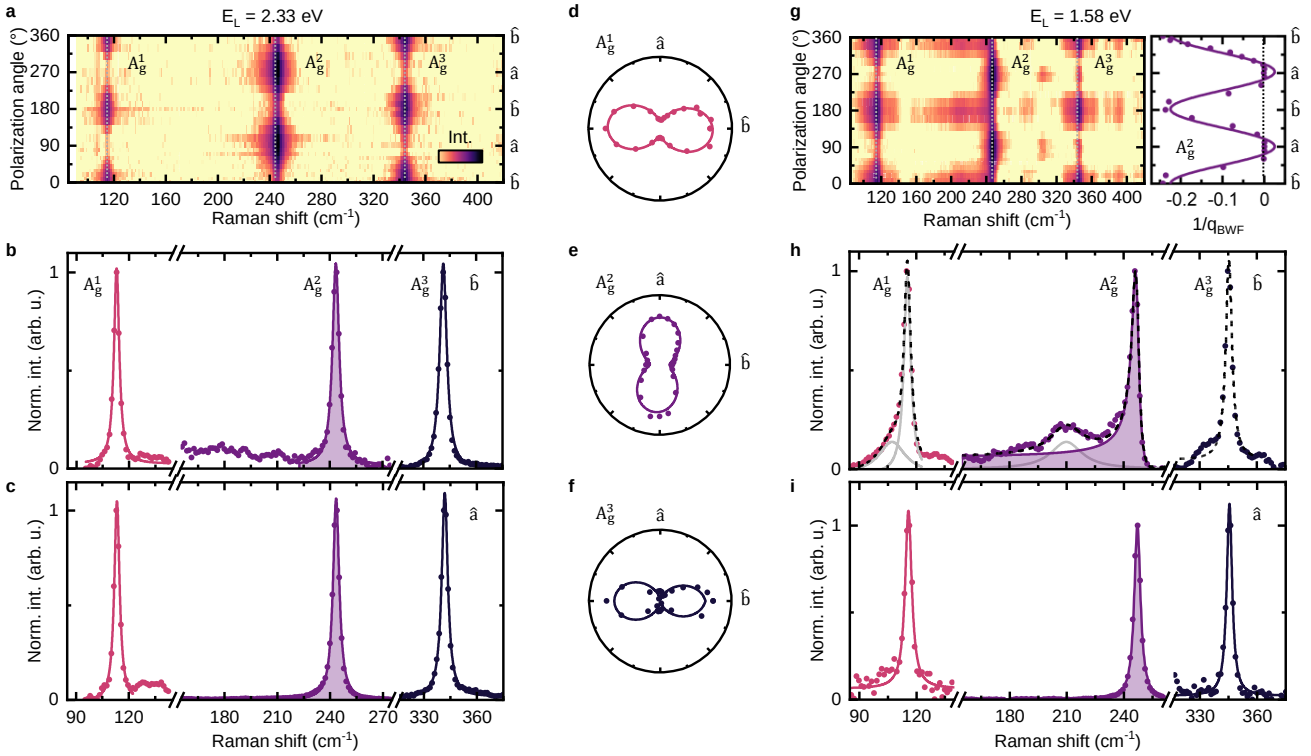

FIG.| 2. **Resonant and non-resonant Raman spectroscopy in bulk CrSBr. a**, False color mapping of the polarization angle dependent Raman spectra with off-resonant excitation at $E_L = 2.33\,\mathrm{eV}$ far above the single-particle gap. The three main phonon modes A_g^1 ($115\,\mathrm{cm}^{-1}$), A_g^2 ($245.5\,\mathrm{cm}^{-1}$) and A_g^3 ($344\,\mathrm{cm}^{-1}$) in CrSBr are highlighted. **b**, Raman spectrum with polarization along the b-direction (b̂, 0° or 180°) shows Lorentzian line shapes as does **c** the a-direction (â, 90° or 270°). **d-f**, Polarization angle dependent intensity of the A_g^1, A_g^2 and A_g^3 phonon mode for excitation at $E_L = 1.58\,\mathrm{eV}$. Only mode A_g^2 exhibits an intensity maximum along the â-direction. **g**, Left: Polarization dependent Raman at an excitation energy of $E_L = 1.58\,\mathrm{eV}$ that is in electronic resonance with the band gap. Right: The Breit-Wigner-Fano coupling parameter $1/q_{BWF}$ of the A_g^2 phonon mode oscillates between the b- and a-direction as further indicated by the sine fit. **h**, Raman spectrum with the electric field co-polarized along the b-direction. The A_g^2 mode is fitted with a BWF resonance (see Eq. 1). **i**, Raman spectrum along the a-direction. All modes exhibit fully Lorentzian lineshapes.

disorder-related effects such as strain, unintentional doping from the substrate, defects or adsorbates. For bulk CrSBr, we obtain Lorentzian linewidths of the 1s exciton of $\sim$ 1 meV, reminiscent of high-quality hBN encapsulated TMDCs. [41, 42]

Quasi-1D electron-phonon coupling. The quasi-1D electronic structure and band anisotropy is expected to manifest itself in the quasi-particle excitations and their mutual interactions. To explore such interactions between excitations of the 2D lattice and excitations of the quasi-1D electronic system, we perform resonant inelastic light scattering (RILS) spectroscopy. [43] In order to selectively probe the quasi-particles of the lattice excitations, we use non-resonant Raman with an excitation well above the band gap of $E_L = 2.33\,\mathrm{eV}$; in order to study the interaction between the quasi-particles' electronic inter-band and lattice excitations, e.g. electron-phonon and exciton-phonon, we perform resonant Raman with excitation close to the single-particle band edge of CrSBr ($E_L = 1.58\,\mathrm{eV}$). For the measurement, we co-align linear excitation and detection polarizations and collect spectra of a bulk CrSBr flake ($\sim 20\,\mathrm{nm}$) as a function of orientation with respect to the crystal axes.

The contour map for non-resonant excitation ($E_L = 2.33\,\mathrm{eV}$) shows three main modes that we identify as the A_g^1 ($115\,\mathrm{cm}^{-1}$), A_g^2 ($245.5\,\mathrm{cm}^{-1}$) and A_g^3 ($344\,\mathrm{cm}^{-1}$) modes (see Fig. 2a). While all modes are due to out-of-plane atomic displacements, the A_g^1 and A_g^3 modes exhibit an intensity maximum along the b-direction while the A_g^2 mode exhibits a maximum along the a-direction (see Fig. 2d-f). Importantly, the lineshape of all modes is Lorentzian for all polarization angles.

For resonant excitation ($E_L = 1.58\,\mathrm{eV}$), we observe a number of additional resonant modes with distinct energies and a very pronounced asymmetric Fano line shape of the A_g^2 mode (see Fig. 2g-i) but only when the electric field vector is aligned along the b-direction (k-vector pointing along the a-direction). This line shape is a hallmark signature for the presence of resonance effects, e.g.

coupling between lattice and electronic excitations. [3, 4] We attribute this to the strong polarization-selective 1D-like electron-phonon interaction of the A_g^2 mode with the electronic structure of CrSBr. The A_g^2 is polarized along the a-direction and is therefore prone to strongly couple to the high DOS of the electronic system along the $\Gamma - X$ direction (see Fig. 1c). This is known as a Breit-Wigner-Fano (BWF) resonance with the phonon as discrete state and the 1D DOS along the a-direction as the electronic continuum from shallow 1D quantum confinement. [3, 4] The spectral form of a BWF resonance is given by

$$I(\omega) = I_0 \frac{[1 + (\omega - \omega_{BWF}/q_{BWF}\Gamma)]^2}{1 + [(\omega - \omega_{BWF})/\Gamma]^2} \qquad (1)$$

where the asymmetry factor $1/q_{BWF}$ characterizes the coupling strength between the phonon and the electronic continuum and ω_{BWF} is the uncoupled BWF peak frequency. The BWF resonance profile reproduces the experimental A_g^2 mode spectrum under resonant excitation along the b-direction (see Fig. 2b). The BWF coupling parameters $1/q_{BWF}$ deduced from those fits (see right panel Fig. 2g) reveal a high coupling strength between phonons and electronic continuum of $1/q_{BWF} = -0.24$ for polarization along the b-direction that is comparable with reports on metallic CNTs with values between -0.2 and -0.6. [6–8] In contrast, the line shape of the RILS spectra of A_g^2 measured along the a-direction is best described by a pure Lorentzian with $1/q_{BWF}$ yielding vanishing coupling between phonons and the electronic continuum. The observation of the highly anisotropic Fano resonance is a strong signature for the 1D nature of the continuum. [6–8]

The observed 1D nature of the electronic system in the 2D van der Waals material with even 3D spin exchange interaction is highly unexpected. We can understand the behavior by the flat conduction band along the $\Gamma - X$ direction with its very large DOS (see Fig. 1c). Under the assumption that the lattice excitations (phonons) couple to the highly anisotropic electronic continuum (collective excitations of electrons), we expect the BWF coupling term (between the electronic continuum and the discrete phonon line) to be proportional to the DOS at E_F. Using the 1D model for carrier dynamics (see SI), we can estimate this DOS to be $\nu(E) = \sqrt{\frac{2m^*}{E}}\frac{1}{2\pi\ell}$ where m^* is the effective mass in the dispersive direction, ℓ is the effective interchain distance, and E is the energy relative to the conduction band minimum. For carrier density n_{el}, we find that this DOS scales as $\nu(E_F) \sim \frac{m^*}{\pi^2\ell^2 n_{\mathrm{el}}}$, yielding a large number of electron-hole excitations which can hybridize with the phonon mode.

Quasi-1D excitons in CrSBr. CrSBr exhibits a rich optical spectrum with several peaks that are not yet identified. [29, 34] The quasi-1D electronic structure of CrSBr is expected to directly affect the properties of the Coulomb bound quasi-particle excitations. To provide more understanding to the complex optical spectrum and the implications that arise from the quasi-1D electronic structure, we calculate excitonic properties of monolayer CrSBr based on DFT+GW and Bethe-Salpeter equations (BSE) and compare them with experimental signatures from optical PL and reflectivity measurements. Results for the calculated excitonic spectrum are shown for the electric field polarized along the b- and the a-directions (see Fig. 3a and b). We identify four excitonic resonances in the b-direction: $\Omega_1 = 1.22\,\mathrm{eV}$, $\Omega_2 = 1.24\,\mathrm{eV}$, $\Omega_3 = 1.87\,\mathrm{eV}$ and $\Omega_4 = 1.93\,\mathrm{eV}$. The two energetically lowest excitons are split by only $\Delta E = 20\,\mathrm{meV}$. This energy difference has its origin in the two energy split conduction bands (see inset Fig. 1c). We obtain large binding energies for $E_b(\Omega_1) = 0.88\,\mathrm{eV}$ and $E_b(\Omega_2) = 0.90\,\mathrm{eV}$. The corresponding real-space representation of the excitonic wavefunctions of Ω_1 and Ω_2 suggest a strong 1D character with the excitons extended along the b-direction but squeezed along the a-direction (see Fig. 3c). The origin is the predominant orbital admixture from the flat conduction bands along the $\Gamma - X$ direction (see Fig. 3d). For the most important orbitals we obtain an admixture for the upper conduction band of 61% $d_{(x^2-y^2)}$, 10% $d_{(3z^2-r^2)}$, 27% p_z and for the lower conduction band of 61% $d_{(x^2-y^2)}$, 25% $d_{(3z^2-r^2)}$, 7% p_z. Importantly, the anisotropy can not only be found in the effective electron mass along $\Gamma - X$ and $\Gamma - Y$, but also dominates the dielectric function $\epsilon^{2D}(q_x, q_y)$ in reciprocal space (see Fig. 3e and f). It is this intricate interplay of effective mass anisotropy and dielectric anisotropy that shows in the quasi-1D character of the excitonic quasi-particles in CrSBr.

We now probe the excitonic signatures of bulk CrSBr at low temperature (4.2 K) by non-resonantly exciting the system with a continuous-wave laser at an energy of 2.384 eV (see Fig. 3g). We observe that the 1s exciton at an energy of $\sim$ 1.366 eV (at an excitation power of 10 µW) appears as a doublet, likely due to a cavity effect (interference effects) caused by the finite thickness of the crystal ($\sim$ 36.8 nm) (see SI). We obtain a very sharp Lorentzian peak with a full width at half maximum (FWHM) of $\sim$ 1 meV verifying high homogeneity of the parallel weakly coupled chains in combination with the high crystal quality. The 1s exciton red-shifts with increasing excitation power typically observed for increasing number of photo-generated carriers in other semiconducting van der Waals materials (also see SI). [44] Moreover, for high excitation powers, additional resonances above the 1s exciton, labelled X^* and X^{**}, appear at energies of 1.380 eV and 1.391 eV, respectively. While they are weakly visible in PL, their appearance in the derivative of the low-temperature (1.6 K) differential reflectivity measurements (see Fig. 3h) suggests finite oscillator strength and band related transitions. The energy split-

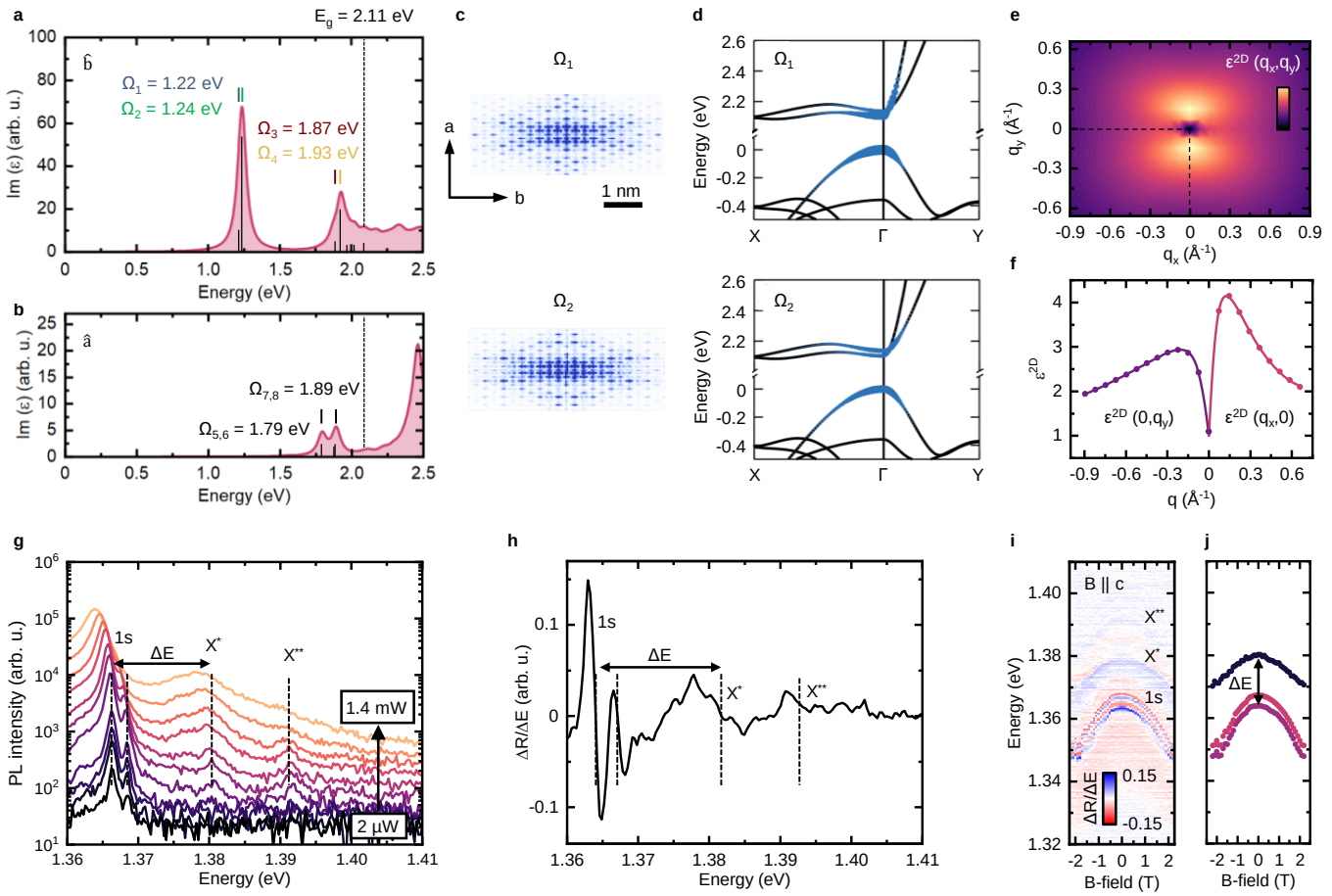

FIG.| 3. **Excitons with quasi-1D electronic character from dielectric and mass anisotropy in CrSBr. a**, Calculated optical absorption spectrum from ab initio by solving the BSE of 1L CrSBr for an electric field polarized along the b-direction (Y-direction). The spectrum shows four excitonic resonances. Ω_1 and Ω_2 originate from the two split conduction bands with a small energy splitting of $\Delta E_{\Omega_1,\Omega_2} \sim 20\,\text{meV}$. The binding energies are given by 0.88 eV and 0.90 eV for Ω_1 and Ω_2, respectively. Ω_3 and Ω_4 are excitons from energetically higher lying bands. **b**, Calculated optical absorption spectrum from ab initio BSE of 1L CrSBr for the electric field polarized along the a-direction (X-direction) showing the strong electronic anisotropy and the absence of Ω_1 and Ω_2. **c**, Corresponding anisotropic real space exciton wavefunction of Ω_1 and Ω_2. **d**, Momentum space exciton composition of Ω_1 and Ω_2 have large band contribution along the $\Gamma - X$ direction. **e**, Calculated macroscopic momentum-dependent dielectric function $\epsilon^{2d}(q_x, q_y)$ of freestanding 1L CrSBr exhibiting a strong anisotropy along q_x and q_y. **f**, $\epsilon^{2d}(0, q_y)$ and $\epsilon^{2d}(q_x, 0)$ as a function of q. First-principle results are symbolized by the dots, while solid lines are a guide to the eye. **g**, Low-temperature (4.2 K) PL as a function of excitation power of bulk CrSBr. The spectrum shows a double resonance for the 1s exciton ($\sim 1.366\,\text{eV}$) due to the finite thickness of the flake ($\sim 36.8\,\text{nm}$) and two signatures X^* and X^{**} at 1.380 eV and 1.391 eV, respectively. The energy splitting between the 1s exciton and X^* is $\Delta E \sim 15\,\text{meV}$. **h**, Derivative of the differential reflectivity $\Delta R/\Delta E$ taken at 1.6 K showing the same resonances. **i**, False color plot of the magnetic field dependent differential reflectivity $\Delta R/\Delta E$ with the B-field applied parallel to the c-axis. The data show the 1s exciton, X^* and a faint signature of the X^{**}. **j**, Position of the 1s exciton doublet and X^*.

ting of the 1s exciton and the X^* is only $\Delta E \sim 15\,\text{meV}$.

In order to learn about the impact of the magnetic order and exchange interaction between the magnetic moments in the 3D matrix and the quasi-1D excitons and their potential origin, we probe the 1s exciton, X^* and X^{**} at 1.6 K in reflectivity as a function of a magnetic field along the c-axis (see Fig. 3i). The signatures show the expected magnetic field-dependent energy shift due to the change in magnetic ordering from AFM to FM until reaching the coercive field of 2 T (see Fig. 3j). The energy shift of the X^* is weaker as compared to the 1s exciton. The X^{**} is weak in signal for higher fields but suggests a qualitatively similar energy shift as the X^* (see Fig. 3i).

The attribution of the X^* and X^{**} is non-trivial. Potential scenarios would involve momentum direct or indi-

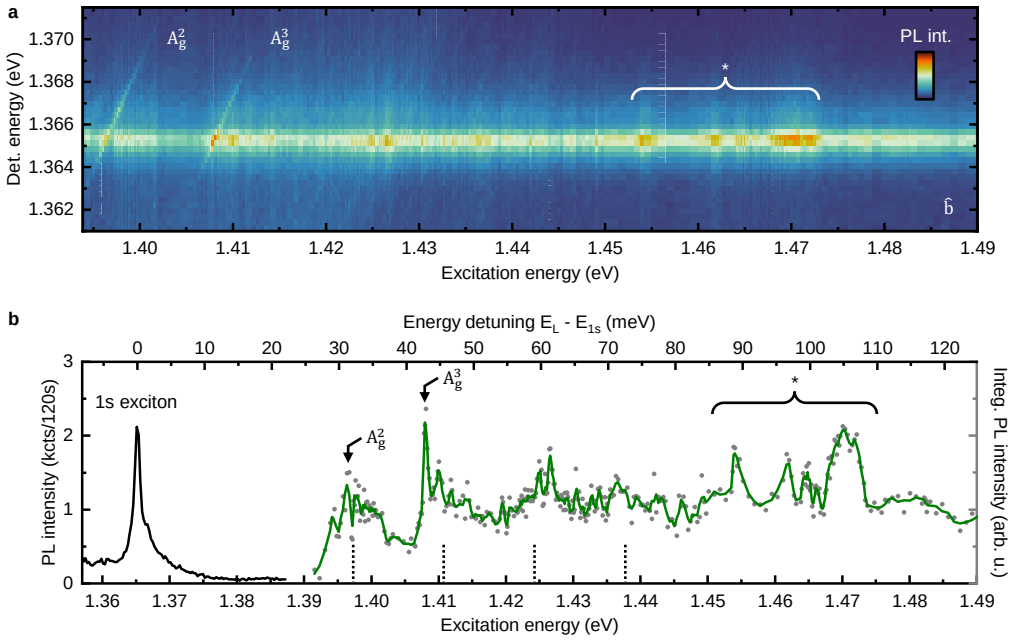

FIG.| 4. **Pronounced exciton-phonon coupling and rich electronic structure in bulk CrSBr. a**, False color low-temperature (4.2 K) PLE mapping of the 1s exciton at an emission energy of $\sim$ 1.365 eV. The 1s exciton shows resonant exciton-phonon coupling with two discrete phonons (A_g^2 and A_g^3) and additional electronic resonances highlighted with arrows. **b**, PL emission spectrum of the 1s exciton at $E_L = 1.406$ eV. Integrated intensity of the 1s exciton as a function of laser excitation energy. The green line is a moving average to the data. The energies of the A_g^2 and A_g^3 are highlighted. Moreover, the 1s exciton exhibits intensity oscillations that are equidistant in energy with a periodicity of $\sim 12.4 \pm 1.0$ meV (see dashed lines and SI). At higher energies ($E > 1.45$ eV) additional distinct energy resonances ($*$) are observed and highlighted.

rect transitions between the split conduction bands and the valence band. It is indeed a possibility that these transitions are more complex in nature with a momentum indirect character due to the strong extension of the wavefunction along the $\Gamma - X$ direction. Such a transition can furthermore be phonon-assisted.

The energetic shift in the magneto-reflectivity data of the 1s exciton and the X^* and X^{**} suggests that the main orbital composition is likely still from the two split conduction bands. At the Γ point in bulk CrSBr, the orbital composition of the lower conduction band is 59% $d_{(x^2-y^2)}$, 21% $d_{(3z^2-r^2)}$, 10% p_z while for the upper conduction band it is 60% $d_{(x^2-y^2)}$, 5% $d_{(3z^2-r^2)}$, 34% p_z. The upper conduction band has a much lower admixture of Cr $d_{(3z^2-r^2)}$ orbitals which suggests a scenario in which the exciton reacts less to an external magnetic field since the magnetic moment is situated on the d-orbital. This would suggest the potential origin of the X^* and X^{**} from a transition that involves the upper conduction band. In general, the excitonic transitions are expected to inherit the orbital character, also for potential indirect transitions that preserve the orbital conduction band admixture away from the Γ point. This further illustrates that the quasi-1D electronic structure and related orbital admixture have direct consequences on the magneto-optical coupling of the excitonic complexes in CrSBr.

Exciton-phonon coupling and electronic structure of CrSBr. In the last part of this manuscript, we further confirm our interpretation of CrSBr as a quasi-1D quantum material in the bulk limit by studying the electronic structure and quasi-particle interactions of CrSBr using high-resolution PLE measurements. Therefore, we spectroscopically probe CrSBr at low-temperature ($T = 4.2$ K) by tuning a continuous-wave laser in small steps over a wide energy range from 1.39 eV to 1.76 eV and collect the PL from the 1s exciton with excitation and detection co-polarized along the b-direction. Figure 4a shows a false color contour plot of the 1s exciton PL as a function of the excitation energy, with the corresponding integrated 1s exciton intensity shown in Fig. 4b. The PLE measurement exhibits an intricate fine structure with several features and resonances. Two energetic regions are of particular interest. In the energy range ($E < 1.45$ eV) close to the 1s exciton (~ 1.365 eV) phonons play an important role. Here, we observe two distinct lines crossing the 1s exciton PL signal. We interpret these lines as resonant Raman signatures suggesting pronounced exciton-phonon coupling between two discrete phonons with the 1s exciton. Such signatures appear in the spectra when the energy detuning of the laser photon and the 1s exciton equals a phonon or multiple phonon energies, leading to the resonant enhancement of the exciton emission. The two phonon lines cross with the 1s exciton

at energy detunings of $\sim$ 31.1 meV ($\sim$ 249 cm^{-1}) and $\sim$ 42.9 meV ($\sim$ 343 cm^{-1}), respectively. The energies are in excellent agreement with the energies of the A_g^2 and A_g^3 phonon modes (see Fig. 2). Pronounced exciton-phonon coupling effects are usually observed for 2D materials like hBN-encapsulated TMDCs [42, 45] as a consequence of narrow exciton linewidths, intrinsically high oscillator strength and high phonon DOS $\propto q$ [42] but are very pronounced even in our measurement further reflecting the low-dimensional character of CrSBr in the bulk limit.

In the same energy range ($E < 1.45$ eV), we also observe oscillations in the 1s exciton emission intensity with equidistant energies with respect to the 1s exciton emission with a periodicity of 12.4 ± 1.0 meV (99.2 ± 8 cm^{-1}) (see dashed lines in Fig. 4b and SI). This energy is $\sim$ 15% lower than the A_g^1 phonon mode energy (14.3 meV) (see Fig. 2). We interpret the equidistant features as exciton-phonon bound states. The observation of optically dark phonon replica energetically above the 1s exciton has been recently observed in $NiPS_3$ [46, 47] and interpreted as optically dark magnetic bound exciton-phonon states. A reduced energy of this bound state is expected for [46, 48] and further illustrates the strong orbital and quasi-particle interactions in bulk CrSBr due to the reduced dimensionality.

Finally, for higher energy detunings ($E > 1.45$ eV), we observe a sequence of additional resonances in the 1s exciton emission that are energetically close to the single-particle gap (see peaks labelled with * in Fig. 4a and b). In this energy range, Rydberg states can be expected in bulk CrSBr. In general, the anisotropic, quasi-1D screening is expected to result in a divergence of the 1s state, increasing the energy splitting between the 1s and 2s state. While our results provide initial insights into the complex electronic structure of CrSBr, additional measurements and theory are required to understand potential excited states in this material.

Conclusion and Outlook. We have provided strong experimental and theoretical evidence that bulk CrSBr is a quasi-1D quantum material. The quasi-particles in CrSBr and their mutual couplings illustrate the 1D character electronic that offers very clean experimental signatures in addition to the magnetic order. We find that this material represents an exciting new platform to study the physics of quasi-1D electronic systems that are highly interacting with vibrational, optical, excitonic and magnetic degrees of mixed dimensionalities.

The energetic flat band along the a-direction motivates more detailed studies of potential correlated behaviors in this material. Generally, 1D systems are known to have strong tendencies towards charge density-wave order via Peierls instability, which is consistent with the observation of pronounced electron-phonon interaction in this system. While this is a strong possibility, it is also possible that at low densities other phases may compete and be favored. In particular, since the Coulomb interaction is long-ranged in the absence of free carriers, it is possible that at low carrier densities, the system may instead tend towards a 1D Wigner crystal [49] or a stripe phase, [50, 51] given that the kinetic energy is already largely quenched in 1D, while the Coulomb interaction remains long-range (see theoretical considerations in the SI).

CrSBr is a fascinating material that exhibits a very intriguing electronic structure. The rich magnetic phase diagram contributes additional complexity rendering it an ideal platform for exploring fundamental physics and exciting new applications. We believe that the 1D electronic character is a universal feature of the chalcogenhalide materials and signatures of this are likely to be expected in other related compounds.

METHODS

Crystal growth and sample fabrication

CrSBr bulk crystals were grown by chemical vapor transport. [31] Samples were fabricated by mechanical exfoliation onto SiO_2/Si substrates. Sample thickness was verified by a combination of atomic force microscopy, optical phase contrast and Raman spectroscopy.

Raman spectroscopy

Resonant and non-resonant Raman measurements were performed on a Renishaw inVia micro-Raman confocal microscope. For the measurements we used a 100x objective with a laser spot size of ~ 1 µm. The laser excitation power used for the measurements taken at 785 nm and 532 nm was 1000 µW and 250 µW, respectively. Ten individual spectra acquired at 20 s were averaged resulting in a spectrum with a total integration time of 200 s. To adjust the polarization we used a linear polarizer in the excitation and detection path that we co-polarized. To change the polarization angle, the sample was placed on a rotating stage.

Photoluminescence spectroscopy

For the PL measurements, we mounted the sample in closed-cycle helium cryostats (Montana Instruments or AttoDry 800) with a base temperature of 4.2 K. In both setups, measurements were made through the side window using a home-built confocal microscope with a $\times$100, 0.9 NA objective (Olympus). We excited the sample using a continuous-wave (CW) laser at 2.384 eV or 1.746 eV. The PL is collected confocally after using a long-pass filter. For the polarization resolved PL, we used a linear polarizer in both excitation and detection and

a half-wave plate to rotate the polarization. The light was fiber-coupled and directed to a high-resolution spectrometer that was attached to a liquid nitrogen cooled charge-coupled device camera.

Photoluminescence excitation spectroscopy

For the PLE measurements we used a tunable CW Ti:Sapphire laser (MSquared Solstis) that is highly monochromatic with a linewidth of 10^{-6}nm. The wavelength is locked using a wavemeter (High Finesse WS8). After wavelength tuning, we adjusted the excitation power to 100 µW before the microscope objective. Measurements were taken with the half-wave plate rotated such that the electric field pointed along the *b*-direction. The light was fiber-coupled and subsequently dispersed using a high-resolution spectrometer attached to a liquid nitrogen cooled charge-coupled device camera.

Magneto-optical spectroscopy

For the magnetic field-dependent optical measurements we mounted CrSBr bulk flakes on top of a SiO_2/Si substrate into a closed-cycle cryostat (attodry 2100). We cooled the sample to a lattice temperature of around 1.6 K. The magnetic field of a superconducting solenoid magnet is aligned along the *c*-axis of the crystal, with a maximum field up to 9 T. We fiber-coupled a broadband light source on the input to perform magnetic field-dependent reflectance measurements. The signal from the sample was collected using a second fiber and directed towards a high-resolution spectrometer attached to a liquid nitrogen-cooled charge-coupled device camera. The broadband laser excitation power was set to 100 µW.

Scanning tunneling microscopy

The topographic images were taken at room temperature with a Unisoku UHV-LT four-probe scanning tunnelling microscope operated with a Nanonis controller. The CrSBr bulk crystal was cleaved in under vacuum to obtain a clean sample surface. The STM is equipped with a scanning electron microscope to allow precise location of scan areas. We acquired differential conductance (dI/dV) spectra using a lock-in amplifier. During data acquisition, the feed back loop was switched off. The data were acquired with PtIr tips.

Scanning transmission electron microscopy

STEM imaging was performed with a probe-corrected Thermo Fisher Scientific Themis Z G3 operated at 200 kV. The probe convergence semi-angle was 19 mrad. The corresponding probe size of the aberration-corrected electron beam is sub-Angstrom. The beam current was 60 pA.

Many-body perturbation theory: *GW*+BSE

CrSBr exhibits spin-orbit coupling and inplane ferromagnetism. To calculate its electronic ground state from first principles, we have employed density functional theory (DFT) in the generalized gradient approximation (GGA) [52]. The correct spin structure is provided by the noncollinear DFT formalism [53, 54]. This provides the wavefunction as spinors and is a good starting point for many-body perturbation theory, which straightly includes all effects of noncollinear magnetism as well.
On top of DFT, we have calculated the quasi-particle (QP) band structures by including the self energy $\Sigma(E)$ in the *GW* approximation [55]. Here, the one-particle Green's function G and the screened Coulomb interaction W (including the dielectric response in random phase approximation) are derived and $\Sigma = iGW$ replaces the DFT exchange correlation energy V_{xc}. The Hamiltonian becomes

$$H^{\mathrm{QP}} = H^{\mathrm{DFT}} + iGW - V_{\mathrm{xc}} \tag{2}$$

where the resulting difference is the quasi-particle correction Δ^{QP} from many-body perturbation theory. The QP band structure energies are then given by

$$E^{\mathrm{QP}}_{n\mathbf{k}} = E^{\mathrm{DFT}}_{n\mathbf{k}} + \langle \psi^{\mathrm{DFT}}_{n\mathbf{k}} | \Sigma(E^{\mathrm{QP}}_{n\mathbf{k}}) - V_{\mathrm{xc}} | \psi^{\mathrm{DFT}}_{n\mathbf{k}} \rangle \tag{3}$$

While often the one-shot *GW* is evaluated only accounting for the diagonal terms of Σ (and Δ^{QP}, respectively), this is not sufficient for CrSBr (see e.g. [56–58]). Therefore, we calculate the QP wavefunctions as linear combination of the DFT wavefunctions

$$\psi^{\mathrm{QP}}_{m\mathbf{k}} = \sum_n D^n_{m\mathbf{k}} \psi^{\mathrm{DFT}}_{n\mathbf{k}} \ . \tag{4}$$

where the coefficients $D^n_{m\vec{k}}$ are given by the solution of the full eigenvalue problem

$$\sum_{n'} H^{\mathrm{QP}}_{nn'} \left(\mathbf{k}; E^{\mathrm{QP}}_{m\mathbf{k}}\right) D^{n'}_{m\mathbf{k}} = E^{\mathrm{QP}}_{m\mathbf{k}} D^n_{m\mathbf{k}} \ . \tag{5}$$

For further details see [58]. Because of the large changes of the band gap, we use a scissor operator to anticipate its opening and thus accelerates the self-consistent determination of QP shifts. For monolayer, bilayer and bulk we employ 1.4 eV, 1.1 eV and 1.0 eV, respectively.

In GW we represent all the two-point functions (P, ϵ, W) by a hybrid basis set of Gaussian orbitals with decay constants ranging from 0.14 to 5.1 a_B^2 and plane waves with an energy cutoff set to 1.5 Ry. We apply a k-point sampling of $17 \times 13 \times 1$ point in the first Brillouin zone. For the BSE we increased the sampling to $32 \times 24 \times 1$ points. For the resulting spectra (Fig. 3a and b) an artificial broadening of 35 meV is applied.

Macroscopic momentum-dependent dielectric function

To obtain the nonlocal macroscopic dielectric function in Fig 3 we calculate the head element of the dielectric matrix in the static limit $\varepsilon^{2d}(\mathbf{q}) := \varepsilon_{\mathbf{G}=0,\mathbf{G}'=0}(\mathbf{q})$ using BerkeleyGW [59, 60] with 2-d Coulomb truncation [61]. To this end, spin-polarized density functional theory (DFT) calculations are carried out using Quantum Espresso [62, 63]. We apply the generalized gradient approximation (GGA) by Perdew, Burke, and Ernzerhof (PBE) [64, 65] and use optimized norm-conserving Vanderbilt pseudopotential [66] at a plane-wave cutoff of 80 Ry. Uniform meshes with $24 \times 18 \times 1$ k-points are combined with a Fermi-Dirac smearing of 5 mRy. A large vacuum of 28Å with a truncated Coulomb interaction [67] is included between repeated supercells in c-axis direction. The calculations are performed using the same lattice structure and band gap as in the electronic ground state calculation for our DFT+GW approach.

Charge density calculations

The charge density calculations shown in Fig. 1g and h were performed using the PWmat package. SG15 pseudopotential and HSE exchange correlation functional were used. A plane wave energy for the basis set is cut off up to 50 Ry. The charge density shown includes the states in the range 0.1 eV below the top of the valence band and 0.1 eV above the bottom of the conduction band.

ACKNOWLEDGEMENTS

J.K. and M.F. acknowledge support by the Alexander von Humboldt foundation. B.P. is a Marie Skłodowska-Curie fellow and acknowledges funding from the European Union's Horizon 2020 research and innovation programme under the Grant Agreement No. 840968 (COHESiV). F.M.R. acknowledges funding from the U.S. Department of Energy, Office of Basic Energy Sciences, Division of Materials Sciences and Engineering under Award DE-SC0019336 for STEM characterization. Work by J.B.C. and P.N. is partially supported by the Quantum Science Center (QSC), a National Quantum Information Science Research Center of the U.S. Department of Energy (DOE). J.B.C. is an HQI Prize Postdoctoral Fellow and gratefully acknowledges support from the Harvard Quantum Initiative. Z.S. is supported through the Department of Energy BES QIS program on 'Van der Waals Reprogrammable Quantum Simulator' under award number DE-SC0022277 for the work on long-range correlations, as well as partially supported by the Quantum Science Center (QSC), a National Quantum Information Science Research Center of the U.S. Department of Energy (DOE) on probing quantum matter. P.N. acknowledges support as a Moore Inventor Fellow through Grant No. GBMF8048 and gratefully acknowledges support from the Gordon and Betty Moore Foundation as well as support from a NSF CAREER Award under Grant No. NSF-ECCS-1944085. M.F. and A.S. were supported through a grant for CPU time at the HLRN (Berlin/Göttingen). Z.Sof. and J.L. were supported by Czech Science Foundation (GACR No. 20-16124J). The optical PL and PLE spectroscopy work at low temperatures was supported by ARO MURI (Grant No. W911NF1810432), HEADS-QON (Grant No. DE-SC0020376), ONR MURI (Grant No. N00014-15-1-2761), CIQM (Grant No. DMR-1231319), and ONR (Grant No. N00014-20-1-2425). Work at CCNY was supported through the NSF QII TAQS (V.M.M.) and the DARPA Nascent Light Matter program (R.B.). F.D. was funded by the Deutsche Forschungsgemeinschaft (DFG, German Research Foundation) through Projektnummer 451072703. M.H., T.D. and M.R. gratefully acknowledge the financial support from German Research Foundation (DFG Project No. DE 2749/2-1), the DFG Collaborative Research Center SFB 1083 (Project No. A13), and computing time granted by the John von Neumann Institute for Computing (NIC) and provided on the supercomputer JUWELS at Jülich Supercomputing Centre (JSC). A.A., J.Q. acknowledge support from a Vannevar Bush Faculty Fellowship, AFOSR DURIP and MURI programs and the Simons Foundation.

AUTHOR CONTRIBUTIONS

J.K. and F.M.R. conceived the project and designed the experiments, J.K. and K.T. prepared the samples, J.K. collected STEM data, J.K. and B.P. performed PL and PLE optical measurements, J.K. and K.T. performed polarization resolved Raman measurements, F.D., R.B. and J.Q., performed magneto-reflectivity measurements, R.D. and J.K. performed STM/STS measurements, Z.Sof. and J.L. synthesized high-quality CrSBr crystals, M.F., M.-C.H., A.S., T.D. and M.R. provided DFT+GW and BSE calculations, J.K. analyzed the experimental data, Z.S., provided charge density

calculations with input from P.N. and furthermore provided the $k \cdot p$ model, J.B.C. provided additional theoretical insights into the correlated physics, M.L., U.W., V.M.M and A.A. discussed results, J.K. wrote the manuscript with input from all co-authors.

ADDITIONAL INFORMATION

Supplementary Information

Three band $k \cdot p$ model; Laser excitation power dependence for different thicknesses; Power dependent exciton red-shift; Photoluminescence excitation spectroscopy of the 1s exciton; Oscillations in the photoluminescence signal of the 1s exciton; One-dimensional correlated phases; Interaction effects (CDW and stripe crystal).

Data availability

The data that support the findings of this study are available from the corresponding author on reasonable request.

Code availability

The codes used for data analysis as well as *ab initio* calculations are available from the corresponding author on reasonable request.

Competing financial interests

The authors declare no competing financial interests.

* jpklein@mit.edu
† prineha@seas.harvard.edu
‡ loncar@seas.harvard.edu
§ fmross@mit.edu

[1] Paredes, B. *et al.* Tonks–girardeau gas of ultracold atoms in an optical lattice. *Nature* **429**, 277–281 (2004). URL https://doi.org/10.1038/nature02530.

[2] Blumenstein, C. *et al.* Atomically controlled quantum chains hosting a tomonaga–luttinger liquid. *Nature Physics* **7**, 776–780 (2011). URL https://doi.org/10.1038/nphys2051.

[3] Rao, A. M. *et al.* Diameter-selective raman scattering from vibrational modes in carbon nanotubes. *Science* **275**, 187–191 (1997). URL https://doi.org/10.1126/science.275.5297.187.

[4] Saito, R., Takeya, T., Kimura, T., Dresselhaus, G. & Dresselhaus, M. S. Raman intensity of single-wall carbon nanotubes. *Physical Review B* **57**, 4145–4153 (1998). URL https://doi.org/10.1103/physrevb.57.4145.

[5] Bockrath, M. *et al.* Luttinger-liquid behaviour in carbon nanotubes. *Nature* **397**, 598–601 (1999). URL https://doi.org/10.1038/17569.

[6] Brown, S. D. M. *et al.* Origin of the breit-wigner-fano lineshape of the tangentialG-band feature of metallic carbon nanotubes. *Physical Review B* **63** (2001). URL https://doi.org/10.1103/physrevb.63.155414.

[7] Nguyen, K. T., Gaur, A. & Shim, M. Fano lineshape and phonon softening in single isolated metallic carbon nanotubes. *Physical Review Letters* **98** (2007). URL https://doi.org/10.1103/physrevlett.98.145504.

[8] Farhat, H. *et al.* Phonon softening in individual metallic carbon nanotubes due to the kohn anomaly. *Physical Review Letters* **99** (2007). URL https://doi.org/10.1103/physrevlett.99.145506.

[9] Lake, B., Tennant, D. A., Frost, C. D. & Nagler, S. E. Quantum criticality and universal scaling of a quantum antiferromagnet. *Nature Materials* **4**, 329–334 (2005). URL https://doi.org/10.1038/nmat1327.

[10] Langer, L. *et al.* Quantum transport in a multiwalled carbon nanotube. *Physical Review Letters* **76**, 479–482 (1996). URL https://doi.org/10.1103/physrevlett.76.479.

[11] Remskar, M. *et al.* Self-assembly of subnanometer-diameter single-wall MoS_2 nanotubes. *Science* **292**, 479–481 (2001). URL https://doi.org/10.1126/science.1059011.

[12] Golberg, D., Bando, Y., Tang, C. & Zhi, C. Boron nitride nanotubes. *Advanced Materials* **19**, 2413–2432 (2007). URL https://doi.org/10.1002/adma.200700179.

[13] Pfeiffer, L. *et al.* Cleaved edge overgrowth for quantum wire fabrication. *Journal of Crystal Growth* **127**, 849–857 (1993). URL https://doi.org/10.1016/0022-0248(93)90746-J.

[14] Meier, S. *et al.* Intersubband excitations in ultrathin core-shell nanowires in the one-dimensional quantum limit probed by resonant inelastic light scattering. *Physical Review B* **104** (2021). URL https://doi.org/10.1103/physrevb.104.235307.

[15] Felser, C., Finckh, E. W., Kleinke, H., Rocker, F. & Tremel, W. Electronic properties of ZrTe3. *Journal of Materials Chemistry* **8**, 1787–1798 (1998). URL https://doi.org/10.1039/a802948b.

[16] Meerschaut, A. & Rouxel, J. Pseudo-one-dimensional MX_3 and MX_4 transition metal chalcogenides. *Springer* 205–279 (1986). URL https://doi.org/10.1007/978-94-009-4528-9_6.

[17] Jin, Y., Li, X. & Yang, J. Single layer of MX3 (M = Ti, Zr; X = S, Se, Te): a new platform for nano-electronics and optics. *Physical Chemistry Chemical Physics* **17**, 18665–18669 (2015). URL https://doi.org/10.1039/c5cp02813b.

[18] Deshpande, V. V., Bockrath, M., Glazman, L. I. & Yacoby, A. Electron liquids and solids in one dimension. *Nature* **464**, 209–216 (2010). URL https://doi.org/10.1038/nature08918.

[19] Furdyna, J. K. Diluted magnetic semiconductors. *Journal of Applied Physics* **64**, R29–R64 (1988). URL https://doi.org/10.1063/1.341700.

[20] Wurstbauer, U., Śliwa, C., Weiss, D., Dietl, T. & Wegscheider, W. Hysteretic magnetoresistance and thermal bistability in a magnetic two-dimensional hole sys-

tem. *Nature Physics* **6**, 955–959 (2010). URL https://doi.org/10.1038/nphys1782.

[21] Gong, C. *et al.* Discovery of intrinsic ferromagnetism in two-dimensional van der waals crystals. *Nature* **546**, 265–269 (2017). URL https://doi.org/10.1038/nature22060.

[22] Huang, B. *et al.* Layer-dependent ferromagnetism in a van der waals crystal down to the monolayer limit. *Nature* **546**, 270–273 (2017). URL https://doi.org/10.1038/nature22391.

[23] Katscher, H. & Hahn, H. Über Chalkogenidhalogenide des dreiwertigen Chroms. *Die Naturwissenschaften* **53**, 361–361 (1966). URL https://doi.org/10.1007/bf00621875.

[24] Göser, O., Paul, W. & Kahle, H. Magnetic properties of CrSBr. *Journal of Magnetism and Magnetic Materials* **92**, 129–136 (1990). URL https://doi.org/10.1016/0304-8853(90)90689-n.

[25] Wang, C. *et al.* A family of high-temperature ferromagnetic monolayers with locked spin-dichroism-mobility anisotropy: MnNX and CrCX (X=Cl, Br, I; C=S, Se, Te). *Science Bulletin* **64**, 293–300 (2019). URL https://doi.org/10.1016/j.scib.2019.02.011.

[26] Wang, H., Qi, J. & Qian, X. Electrically tunable high curie temperature two-dimensional ferromagnetism in van der waals layered crystals. *Applied Physics Letters* **117**, 083102 (2020). URL https://doi.org/10.1063/5.0014865.

[27] Telford, E. J. *et al.* Layered antiferromagnetism induces large negative magnetoresistance in the van der waals semiconductor CrSBr. *Advanced Materials* **32**, 2003240 (2020). URL https://doi.org/10.1002/adma.202003240.

[28] Lee, K. *et al.* Magnetic order and symmetry in the 2d semiconductor CrSBr. *Nano Letters* (2021). URL https://doi.org/10.1021/acs.nanolett.1c00219.

[29] Wilson, N. P. *et al.* Interlayer electronic coupling on demand in a 2d magnetic semiconductor. *Nature Materials* **20**, 1657–1662 (2021). URL https://doi.org/10.1038/s41563-021-01070-8.

[30] Yang, K., Wang, G., Liu, L., Lu, D. & Wu, H. Triaxial magnetic anisotropy in the two-dimensional ferromagnetic semiconductor CrSBr. *Physical Review B* **104** (2021). URL https://doi.org/10.1103/physrevb.104.144416.

[31] Klein, J. *et al.* Atomistic spin textures on-demand in the van der waals layered magnet CrSBr. *arXiv* (2021). URL https://arxiv.org/abs/2107.00037. arXiv:2107.00037.

[32] Telford, E. J. *et al.* Coupling between magnetic order and charge transport in a two-dimensional magnetic semiconductor. *Nature Materials* (2022). URL https://doi.org/10.1038/s41563-022-01245-x.

[33] Wu, F. *et al.* Quasi-1d electronic transport in a 2d magnetic semiconductor. *Advanced Materials* **34**, 2109759 (2022). URL https://doi.org/10.1002/adma.202109759.

[34] Bae, Y. J. *et al.* Exciton-coupled coherent antiferromagnetic magnons in a 2d semiconductor. *arXiv* (2022). arXiv:2201.13197.

[35] Shaz, M. *et al.* Spin-Peierls transition in TiOCl. *Physical Review B* **71** (2005). URL https://doi.org/10.1103/physrevb.71.100405.

[36] Blanco-Canosa, S. *et al.* Enhanced dimerization of TiOCl under pressure: Spin-Peierls to Peierls transition. *Physical Review Letters* **102** (2009). URL https://doi.org/10.1103/physrevlett.102.056406.

[37] Prodi, A., Helton, J. S., Feng, Y. & Lee, Y. S. Pressure-induced spin-peierls to incommensurate charge-density-wave transition in the ground state of TiOCl. *Physical Review B* **81** (2010). URL https://doi.org/10.1103/physrevb.81.201103.

[38] Tran, V. & Yang, L. Scaling laws for the band gap and optical response of phosphorene nanoribbons. *Physical Review B* **89** (2014). URL https://doi.org/10.1103/physrevb.89.245407.

[39] Mak, K. F., Lee, C., Hone, J., Shan, J. & Heinz, T. F. Atomically thin MoSe2: A new direct-gap semiconductor. *Physical Review Letters* **105** (2010). URL https://doi.org/10.1103/physrevlett.105.136805.

[40] Splendiani, A. *et al.* Emerging photoluminescence in monolayer MoS_2. *Nano Letters* **10**, 1271–1275 (2010). URL https://doi.org/10.1021/nl903868w.

[41] Cadiz, F. *et al.* Excitonic linewidth approaching the homogeneous limit in MoS_2-based van der waals heterostructures. *Physical Review X* **7** (2017). URL https://doi.org/10.1103/physrevx.7.021026.

[42] Shree, S. *et al.* Observation of exciton-phonon coupling in MoSe2 monolayers. *Physical Review B* **98** (2018). URL https://doi.org/10.1103/physrevb.98.035302.

[43] Hayes, W. & Loudon, R. *Scattering of light by crystals* (Wiley, New York, NY, 1978).

[44] Steinhoff, A., Rösner, M., Jahnke, F., Wehling, T. O. & Gies, C. Influence of excited carriers on the optical and electronic properties of MoS2. *Nano Letters* **14**, 3743–3748 (2014). URL https://doi.org/10.1021/nl500595u.

[45] Chow, C. M. *et al.* Phonon-assisted oscillatory exciton dynamics in monolayer MoSe2. *npj 2D Materials and Applications* **1** (2017). URL https://doi.org/10.1038/s41699-017-0035-1.

[46] Hwangbo, K. *et al.* Highly anisotropic excitons and multiple phonon bound states in a van der waals antiferromagnetic insulator. *Nature Nanotechnology* **16**, 655–660 (2021). URL https://doi.org/10.1038/s41565-021-00873-9.

[47] Ergeçen, E. *et al.* Magnetically brightened dark electron-phonon bound states in a van der waals antiferromagnet. *Nature Communications* **13** (2022). URL https://doi.org/10.1038/s41467-021-27741-3.

[48] Toyozawa, Y. & Hermanson, J. Exciton-phonon bound state: A new quasiparticle. *Physical Review Letters* **21**, 1637–1641 (1968). URL https://doi.org/10.1103/physrevlett.21.1637.

[49] Schulz, H. Wigner crystal in one dimension. *Physical Review Letters* **71**, 1864 (1993).

[50] Spivak, B. & Kivelson, S. Phases intermediate between a two-dimensional electron liquid and wigner crystal. *Physical Review B* **70**, 155114 (2004).

[51] Emery, V., Fradkin, E., Kivelson, S. & Lubensky, T. Quantum theory of the smectic metal state in stripe phases. *Physical Review Lett.* **85**, 2160 (2000).

[52] Perdew, J. P. *et al.* Atoms, molecules, solids, and surfaces: Applications of the generalized gradient approximation for exchange and correlation. *Physical Review B* **46**, 6671–6687 (1992). URL https://link.aps.org/doi/10.1103/PhysRevB.46.6671.

[53] Stärk, B., Krüger, P. & Pollmann, J. Magnetic anisotropy of thin Co and Ni films on diamond surfaces. *Phys. Rev. B* **84**, 195316 (2011). URL https://link.aps.org/doi/10.1103/PhysRevB.84.195316.

[54] Sandratskii, L. M. Noncollinear magnetism in itinerant-electron systems: Theory and applications. *Advances in Physics* **47**, 91–160 (1998). URL https://doi.org/10.1080/000187398243573.

[55] Hedin, L. New Method for Calculating the One-Particle Green's Function with Application to the Electron-Gas Problem. *Phys. Rev.* **139**, A796–A823 (1965). URL https://link.aps.org/doi/10.1103/PhysRev.139.A796.

[56] Deilmann, T. Valley selectivity induced by magnetic adsorbates: Triplet oxygen on monolayer MoS_2. *Phys. Rev. B* **101**, 085130 (2020). URL https://link.aps.org/doi/10.1103/PhysRevB.101.085130.

[57] Förster, T., Krüger, P. & Rohlfing, M. Two-dimensional topological phases and electronic spectrum of Bi_2Se_3 thin films from *GW* calculations. *Phys. Rev. B* **92**, 201404 (2015). URL https://link.aps.org/doi/10.1103/PhysRevB.92.201404.

[58] Heißenbüttel, M.-C., Deilmann, T., Krüger, P. & Rohlfing, M. Valley-dependent interlayer excitons in magnetic WSe_2/CrI_3. *Nano Letters* **21**, 5173–5178 (2021). PMID: 34077218.

[59] Hybertsen, M. S. & Louie, S. G. Electron correlation in semiconductors and insulators: Band gaps and quasiparticle energies. *Phys. Rev. B* **34**, 5390–5413 (1986). URL https://link.aps.org/doi/10.1103/PhysRevB.34.5390.

[60] Deslippe, J. *et al.* BerkeleyGW: A massively parallel computer package for the calculation of the quasiparticle and optical properties of materials and nanostructures. *Computer Physics Communications* **183**, 1269–1289 (2012). URL https://www.sciencedirect.com/science/article/pii/S0010465511003912.

[61] Qiu, D. Y., da Jornada, F. H. & Louie, S. G. Screening and many-body effects in two-dimensional crystals: Monolayer MoS_2. *Phys. Rev. B* **93**, 235435 (2016). URL https://link.aps.org/doi/10.1103/PhysRevB.93.235435.

[62] Giannozzi, P. *et al.* QUANTUM ESPRESSO: a modular and open-source software project for quantum simulations of materials. *Journal of Physics: Condensed Matter* **21**, 395502 (2009). URL https://doi.org/10.1088/0953-8984/21/39/395502.

[63] Giannozzi, P. *et al.* Advanced capabilities for materials modelling with quantum ESPRESSO. *Journal of Physics: Condensed Matter* **29**, 465901 (2017). URL https://doi.org/10.1088/1361-648x/aa8f79.

[64] Perdew, J. P., Burke, K. & Ernzerhof, M. Generalized Gradient Approximation Made Simple. *Phys. Rev. Lett.* **77**, 3865–3868 (1996). URL https://link.aps.org/doi/10.1103/PhysRevLett.77.3865.

[65] Perdew, J. P., Burke, K. & Ernzerhof, M. Generalized Gradient Approximation Made Simple [Phys. Rev. Lett. 77, 3865 (1996)]. *Phys. Rev. Lett.* **78**, 1396–1396 (1997). URL https://link.aps.org/doi/10.1103/PhysRevLett.78.1396.

[66] van Setten, M. J. *et al.* The PseudoDojo: Training and grading a 85 element optimized norm-conserving pseudopotential table. *Computer Physics Communications* **226**, 39–54 (2018). URL https://www.sciencedirect.com/science/article/pii/S0010465518300250.

[67] Sohier, T., Calandra, M. & Mauri, F. Density functional perturbation theory for gated two-dimensional heterostructures: Theoretical developments and application to flexural phonons in graphene. *Phys. Rev. B* **96**, 075448 (2017). URL https://link.aps.org/doi/10.1103/PhysRevB.96.075448.

The bulk van der Waals layered magnet CrSBr is a quasi-1D quantum material

J. Klein,[1,*] B. Pingault,[2,3] M. Florian,[4] M.C. Heißenbüttel,[5] A. Steinhoff,[6,7] Z. Song,[2] K. Torres,[1] F. Dirnberger,[8] J.B. Curtis,[2] T. Deilmann,[5] R. Dana,[1] R. Bushati,[8,9] J. Quan,[10,11,12,13] J. Luxa,[14] Z. Sofer,[14] A. Alù,[10,11,12,13] V. M. Menon,[8,9] U. Wurstbauer,[15] M. Rohlfing,[5] P. Narang,[2,†] M. Lončar,[2,‡] and F. M. Ross[1,§]

[1] *Department of Materials Science and Engineering, Massachusetts Institute of Technology, Cambridge, Massachusetts 02139, USA*
[2] *John A. Paulson School of Engineering and Applied Sciences, Harvard University, Cambridge, MA, USA*
[3] *QuTech, Delft University of Technology, 2600 GA Delft, The Netherlands*
[4] *Department of Electrical and Computer Engineering, Department of Physics, University of Michigan, Ann Arbor, Michigan 48109, United States*
[5] *Institut für Festkörpertheorie, Westfälische Wilhelms-Universität Münster, 48149 Münster, Germany*
[6] *Institut für Theoretische Physik, Universität Bremen, P.O. Box 330 440, 28334 Bremen, Germany*
[7] *Bremen Center for Computational Materials Science, University of Bremen, 28359, Bremen, Germany*
[8] *Department of Physics, City College of New York, New York, NY 10031, USA*
[9] *Department of Physics, The Graduate Center, City University of New York, New York, NY 10016, USA*
[10] *Department of Electrical and Computer Engineering, The University of Texas at Austin, Austin, TX, 78712, USA*
[11] *Photonics Initiative, CUNY Advanced Science Research Center, New York, NY, 10031, USA*
[12] *Department of Electrical Engineering, City College of the City University of New York, New York, NY, 10031, USA*
[13] *Physics Program, Graduate Center, City University of New York, New York, NY, 10026, USA*
[14] *Department of Inorganic Chemistry, University of Chemistry and Technology Prague, Technická 5, 166 28 Prague 6, Czech Republic*
[15] *Institute of Physics and Center for Nanotechnology, University of Münster, 48149 Münster, Germany*

(Dated: 2022-05-27)

CONTENTS

Three band k·p model 3

Laser excitation power dependence for different thicknesses. 4

Power dependent exciton red-shift 4

Photoluminescence excitation spectroscopy of the 1s exciton. 5

Oscillations in the photoluminescence signal of the 1s exciton. 6

One-Dimensional Correlated Phases 7

Interaction Effects 8
CDW 8
Stripe Crystal 9

References 10

THREE BAND K·P MODEL

Monolayer CrSBr holds space group 59. The direct optical absorption in CrSBr is predominantly around the Γ-point. At the Γ-point, the valence band transforms as the B_{3g} irreducible representation, and the first conduction band transforms as the A_g irreducible representation. According to the symmetry, we build a three-band $k \cdot p$ model around the Γ point in the space spanned by the basis set of ($|B_{1u}\rangle$,$|A_g\rangle$,$|B_{3g}\rangle$). The perturbation is kept up to the second order term. The resulting Hamiltonian is as follows

$$\hat{H} = \begin{pmatrix} E_2 + \frac{\hbar^2 k^2}{2m_e} & 0 & \frac{\hbar k_y p_y}{m_e} \\ 0 & E_1 + \frac{\hbar^2 k^2}{2m_e} + \frac{\hbar^2 k_y^2}{m_2^2}\frac{p_y^2}{E_2 - E_0} & 0 \\ \frac{\hbar k_y p_y}{m_e} & 0 & E_0 + \frac{\hbar^2 k^2}{2m_e} + \frac{\hbar^2 k_y^2}{m_2^2}\frac{p_y^2}{E_0 - E_2} \end{pmatrix}. \tag{1}$$

Here $p_y = \langle B_{3g}|\, \hat{p_y}\, |B_{1u}\rangle$. For the modelling we used an energy splitting in the conduction band of $\Delta_{E_2-E_1} = 33\,\mathrm{meV}$ and $p_y = -1.5 e V m_e/\hbar$. The $k \cdot p$ band structure is in good accordance to the calculated DFT-GW band structure (see SI Fig. 1a and b) and captures particularly the electronic anisotropy.

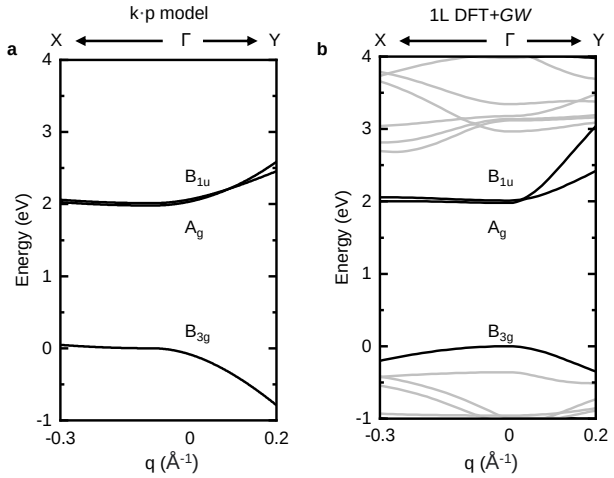

SI Fig.| 1. Comparison between three band $k \cdot p$ model and DFT+GW calculated band structure for monolayer CrSBr around the Γ-point. a, Three band $k \cdot p$ band structure modelled around the Γ-point as obtained from SI Eq. 1 **b**, Calculated DFT+GW band structure of 1L CrSBr.

LASER EXCITATION POWER DEPENDENCE FOR DIFFERENT THICKNESSES.

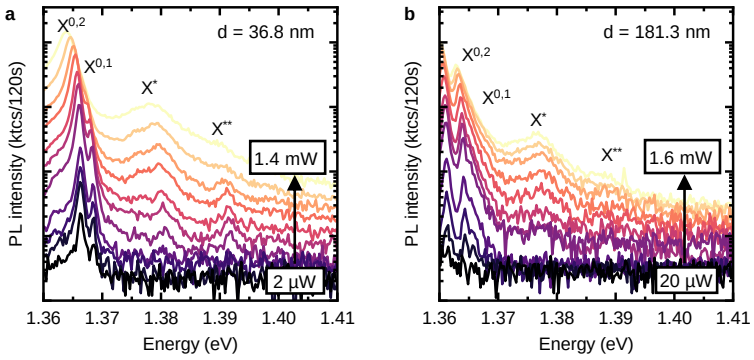

SI Fig.| 2. **Excitation power dependent PL of bulk CrSBr of different thickness. a**, Power dependence of bulk CrSBr with a thickness of $36.8\,\mathrm{nm}$. The PL exhibits the 1s exciton that shows a double peak ($X^{0,1}$ and $X^{0,2}$) and two additional resonances X^* and X^{**}. **b**, Power dependence of bulk CrSBr with a thickness of $181.3\,\mathrm{nm}$. The 1s exciton is split into three peaks, likely due to interference effects from the finite thickness of the material. However, the resonances X^* and X^{**} are unchanged and appear at the approximately same energy difference with respect to the 1s exciton.

POWER DEPENDENT EXCITON RED-SHIFT

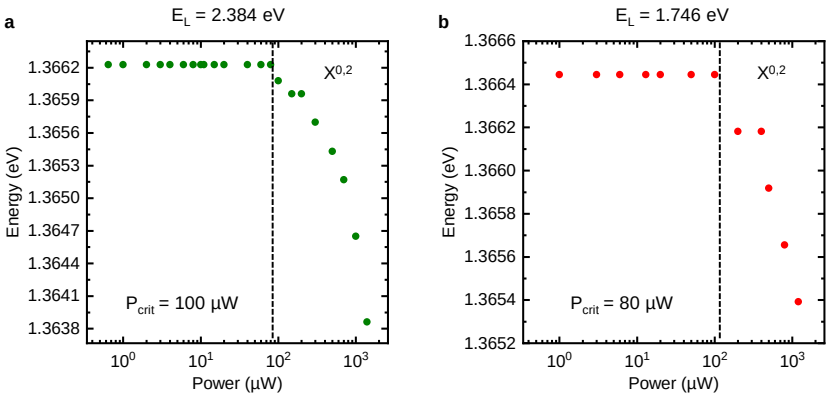

SI Fig.| 3. **Power dependent exciton red-shift. a**, Exciton peak position as a function of laser excitation power for an excitation energy of $2.384\,\mathrm{eV}$. The exciton red-shifts at a critical power of $P_{crit} \sim 100\,\mu\mathrm{eV}$. **b**, Exciton peak position as a function of laser excitation power for an excitation energy of $1.746\,\mathrm{eV}$. The exciton red-shifts at a critical power of $P_{crit} \sim 80\,\mu\mathrm{eV}$.

PHOTOLUMINESCENCE EXCITATION SPECTROSCOPY OF THE 1S EXCITON.

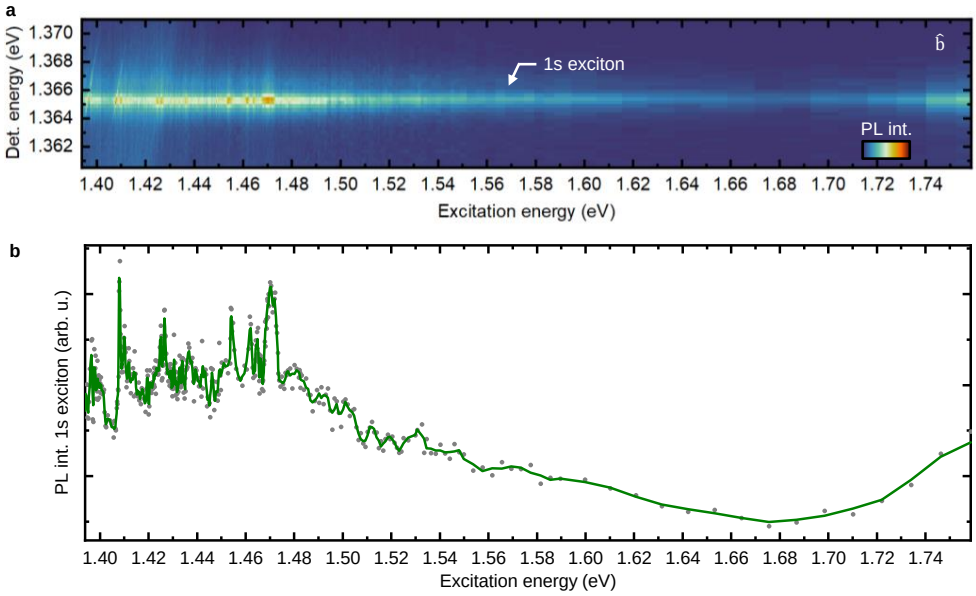

SI Fig.| 4. **Excitation laser energy dependent intensity of the 1s exciton of bulk CrSBr. a**, Spectrally integrated PL intensity of the 1s exciton for the laser energy tuned from $1.39\,\mathrm{eV}$ to $1.76\,\mathrm{eV}$. The solid line is a moving average to the data. **b**, Spectrally integrated intensity of the 1s exciton emission. The solid green line is a moving average to the data. The intensity decreases until reaching a minimum at $\sim 1.68\,\mathrm{eV}$ and increases towards higher energies due to contributions from higher lying bands.

OSCILLATIONS IN THE PHOTOLUMINESCENCE SIGNAL OF THE 1S EXCITON.

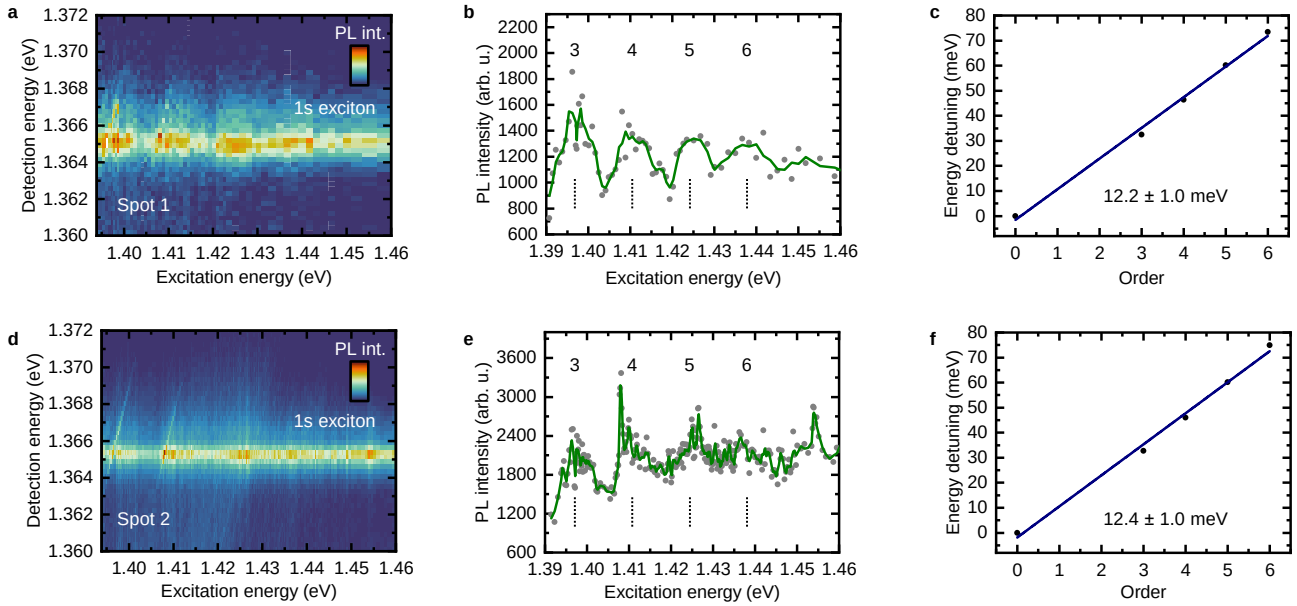

SI Fig.| 5. **Photoluminescence excitation spectroscopy of the 1s exciton in bulk CrSBr. a**, False color mapping of the excitation laser energy dependent spectral response of the 1s exciton at a sample temperature of $4.2\,\mathrm{K}$. The laser energy is tuned from $1.39\,\mathrm{eV}$ to $1.46\,\mathrm{eV}$ with larger energy steps. The 1s exciton exhibits intensity oscillations with equidistant energy spacing. **b**, Spectrally integrated intensity of the 1s exciton emission. The solid line is a moving average to the data. The order of the oscillations is highlighted. **c**, Corresponding energy position of the oscillations plotted as a function of energy detuning with respect to the 1s exciton. The solid line is a linear fit to the data resulting in a slope of $12.2 \pm 1.0\,\mathrm{meV}$ ($97.8 \pm 8.0\,\mathrm{cm}^{-1}$). This energy is 15% smaller as compared to the energy of the A_g^1 phonon mode. Equidistant replica energetically above the 1s exciton have been observed in $NiPS_3$. [1, 2] The features have been attributed to optically dark bound exciton-phonon states. **d**, False color mapping of the excitation laser energy dependent spectral response of the 1s exciton taken at a second spot on the sample with higher energy resolution. **e**, Spectrally integrated intensity of the 1s exciton emission. The solid line is a moving average to the data. The order of the oscillations is highlighted. **f**, Corresponding energy position of the oscillations plotted as a function of energy detuning with respect to the 1s exciton. The solid line is a linear fit to the data resulting in a slope of $12.4 \pm 1.0\,\mathrm{meV}$ ($99.2 \pm 8.0\,\mathrm{cm}^{-1}$).

ONE-DIMENSIONAL CORRELATED PHASES

We provide additional insights into the potential correlated physics of CrSBr. Below the Curie temperature, this CrSBr exhibits intra-layer ferromagnetic order due to Stoner-type interactions resulting in a spin-polarized band structure. As we described in the main manuscript, the conduction band is highly anisotropic, and is nearly completely flat along one axis ($\Gamma - X$), and dispersive along the other ($\Gamma - Y$). This leads us to a model of the system at low carrier doping of that of weakly coupled electronic chains. The chains are furthermore spin-polarized due to the magnetic order (below the Curie temperature).

We consider a toy model Hamiltonian for the band structure of

$$H = \sum_{\mathbf{p}} c_{\mathbf{p}}^{\dagger} E_{\mathbf{p}} c_{\mathbf{p}} \tag{2}$$

where $c_{\mathbf{p}}^{\dagger}$ creates an electron in the conduction band with momentum $\mathbf{p}$. Because of the large exchange energy, we neglect for the time being the spin minority band, though this may be important once fluctuations in the magnetic order are incorporated.

The dispersion is modeled as

$$E_{\mathbf{p}} = \frac{p_x^2}{2m^*} + t_{\perp}(1 - \cos p_y \ell), \tag{3}$$

where m^* is the effective mass of the conduction band along the dispersive direction, and $t_{\perp}$ is the bandwidth of the interchain tunneling, and ℓ is the interchain separation, on the order of one lattice constant.

We take $t_{\perp}\ell^2 \ll 1/m^*$ so that the band dispersion is highly anisotropic. In the absence of electron interactions, this is already interesting as it implies the possibility for very strong impurity RKKY interactions and other one-dimensional electronic liquid physics. We begin by determining the density of states.

We have the density of states of the conduction band of

$$\nu(E) = \int_{\mathbf{p}} \delta(E - E_{\mathbf{p}}) \sim \frac{1}{\ell} \int \frac{dp_x}{2\pi} \delta(E - p_x^2/2m^*) = \frac{2m^*}{\ell} \frac{2}{2\pi 2\sqrt{2m^* E}} = \sqrt{2m^*/E} \frac{1}{2\pi\ell}, \tag{4}$$

evaluated in the flat band limit. We see the emergence of a prominent van Hove singularity due to the low dimensionality. We also see the factor of $1/\ell$ which is the effective density of chains in the Y-direction (b-direction), and is a very large factor owing to the lattice scale origin.

Based on simple integration of density of states, or in general Luttinger's theorem, we find the area of the filled Fermi surface to be equal to the carrier density

$$2\pi/\ell \times 2k_F = 4\pi^2 n_{\mathrm{el}} \tag{5}$$

in the case of a spin-polarized system. We have as a result the relation

$$k_F = \pi \ell n_{\mathrm{el}} \tag{6}$$

and the Fermi level of

$$E_F = \frac{\pi^2 \ell^2 n_{\mathrm{el}}^2}{2m^*}. \tag{7}$$

We find the density of states at the Fermi level is

$$\nu_F = \frac{m^*}{\pi^2 \ell^2 n_{\mathrm{el}}}. \tag{8}$$

For purposes of estimation, we use the calculated effective mass $m_Y^e = 7.31 m_0$, and take an interchain separation of $\ell = 4$Å.

Since the carrier density is likely to be small in comparison to the chain separation ℓ^2, we expect a very small Fermi level even for appreciable doping. As a result, the interaction effects are likely to be dominated by electron-electron interactions and strong Coulomb energy.

INTERACTION EFFECTS

We now briefly discuss interaction effects. Since the model is effectively single channel due to the ferromagnetic ordering, we have comparatively few possible outcomes. The first is the standard Peierl's instability, resulting in a charge density wave (CDW) order, with density (and possibly therefore also magnetization) oscillations along the dispersive direction. We also briefly discuss the possibility of a second, related instability towards Wigner crystal order at low densities. Finally, we will discuss possible effects due to disorder, which is likely to be highly relevant in the low-dimensional transport.

CDW

For charge density wave order, we consider a model of the free electrons interacting with a phonon mode $b_{\mathbf{q}}$ via

$$H_{\text{int}} = \sum_{\mathbf{p},\mathbf{q}} \frac{g_{\mathbf{p}}(\mathbf{q})}{\sqrt{\text{Vol.}}} \frac{b_{\mathbf{q}} + b^\dagger_{-\mathbf{q}}}{\sqrt{2\Omega_{\mathbf{q}}}} c^\dagger_{\mathbf{p}+\frac{\mathbf{q}}{2}} c_{\mathbf{p}-\frac{\mathbf{q}}{2}} + \sum_{\mathbf{q}} \Omega_{\mathbf{q}} b^\dagger_{\mathbf{q}} b_{\mathbf{q}} \tag{9}$$

where the phonon mode is assumed to be of appropriate symmetry and dispersion, captured by $\Omega_{\mathbf{q}}$. We treat this in a perturbative manner, integrating out the fermionic operators.

We find the phonon propagator is dressed by hybridization with the electron-hole excitations. This results in phonon Green's function, in equilibrium, of

$$D(q) = \frac{2\Omega_{\mathbf{q}}}{(i\omega_m)^2 - \Omega^2_{\mathbf{q}} - \int_p |g_{\mathbf{p}}(\mathbf{q})|^2 \mathscr{G}_0(p + \frac{q}{2}) \mathscr{G}_0(p - \frac{q}{2})}. \tag{10}$$

The ionic effective mass M_{eff} has been absorbed into the coupling constant g.

We carry out the Matsubara sum and analytically continue to obtain

$$D^R(\omega, \mathbf{q}) = \frac{2\Omega_{\mathbf{q}}}{(\omega + i0)^2 - \Omega^2_{\mathbf{q}} + \int_{\mathbf{p}} |g_{\mathbf{p}}(\mathbf{q})|^2 \frac{f(\beta\xi_{\mathbf{p}+\frac{\mathbf{q}}{2}}) - f(\beta\xi_{\mathbf{p}-\frac{\mathbf{q}}{2}})}{\xi_{\mathbf{p}+\frac{\mathbf{q}}{2}} - \xi_{\mathbf{p}-\frac{\mathbf{q}}{2}} - (\omega + i0^+)}}. \tag{11}$$

Here, $f(z) = \frac{1}{2}\tanh(z/2)$ is the Fermi occupation function. To proceed, we need to specify more details about the phonon coupling function, and also numerically integrate the Lindhard function, in general.

We focus on the static response function for the phonons, as this will signal the onset of the Peierl's phase. We have instability when

$$\Omega^2_{\mathbf{q}} = \int_{\mathbf{p}} |g_{\mathbf{p}}(\mathbf{q})|^2 \frac{f(\beta\xi_{\mathbf{p}+\frac{\mathbf{q}}{2}}) - f(\beta\xi_{\mathbf{p}-\frac{\mathbf{q}}{2}})}{\xi_{\mathbf{p}+\frac{\mathbf{q}}{2}} - \xi_{\mathbf{p}-\frac{\mathbf{q}}{2}}}. \tag{12}$$

In the case of a Holstein-type coupling to the density alone, we get $g_{\mathbf{p}}(\mathbf{q}) = g(\mathbf{q})$ and thus find the phase boundary determined by

$$\Omega^2_{\mathbf{q}}/|g(\mathbf{q})|^2 = \chi_0(\mathbf{q}). \tag{13}$$

where here we have introduced the bare static Lindhard function

$$\chi_0(\mathbf{q}) = \int_{\mathbf{p}} \frac{f(\beta\xi_{\mathbf{p}+\frac{\mathbf{q}}{2}}) - f(\beta\xi_{\mathbf{p}-\frac{\mathbf{q}}{2}})}{\xi_{\mathbf{p}+\frac{\mathbf{q}}{2}} - \xi_{\mathbf{p}-\frac{\mathbf{q}}{2}}}. \tag{14}$$

The key observation is that at zero temperature there is a Kohn anomaly in the density-density response due to the perfect nesting with the phonon mode exhibiting extreme softening at $q = 2k_F$ before onset of the CDW transition. We have the Lindhard response at $T = 0$ of (for $q < 2k_F$)

$$\chi_0(q) = \frac{m^*}{\pi\ell|q_x|} \log\left(\frac{2k_F + |q_x|}{2k_F - |q_x|}\right). \tag{15}$$

Note this only depends on q_x in the extreme flat band limit of $t_\perp \to 0$. This has a logarithmic singularity at the nesting wavevector of $2k_F$, which is the origin of the instability. We find as $q \to 2k_F$ from below that $\chi_0(2k_F) \to$

$\frac{m}{\pi\ell 2k_F}\log(2/(1-q/(2k_F))) \to +\infty$. Therefore, the equation $\Omega^2_{2k_F}/|g(2k_F)|^2 = \chi_0(2k_F)$ always has as solution at zero temperature. We also see static screening of $\chi_0(q\to 0) = \nu(E_F)$ which is consistent with a Thomas-Fermi result.

The complication is that CDW order requires temperature $T \ll E_F$. However, we find that E_F also evolves with doping such that we need to solve this more carefully in the $T, n_{\rm el}$ plane. Note that $n_{\rm el}$ is related to the Fermi momentum by

$$k_F = \pi\ell n_{\rm el} \tag{16}$$

so that the density directly sets the wavelength of the CDW. We plot the function

$$\chi_0(q=2k_F,T) = \frac{m^*}{\pi^2\ell^2 n_{\rm el}}\int_{-\infty}^{\infty}\frac{dx}{2x}\left(\tanh\left(\frac{(x+1)^2-1}{4m^*T/(\pi\ell n_{\rm el})^2}\right) - \tanh\left(\frac{(x-1)^2-1}{4m^*T/(\pi\ell n_{\rm el})^2}\right)\right), \tag{17}$$

which depends on temperature relative to the Fermi level, and carrier density which in turn tunes the Fermi level. Note that in the tanh functions we ignore the x^2 term, which amounts to implementing the linearized Fermi surface.

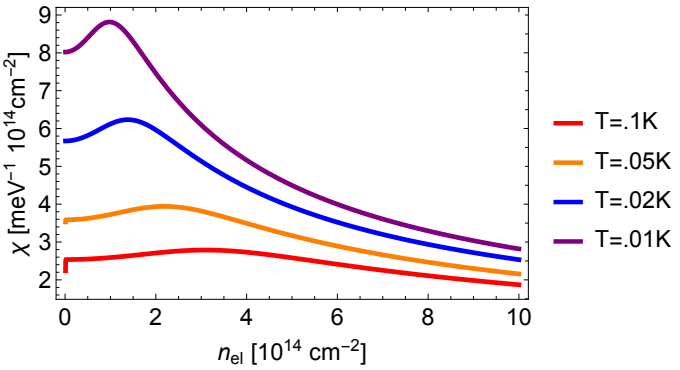

SI Fig.| 6. Lindhard function. Lindhard function at $q = 2k_F$ as a function of carrier density evolving with temperature. The peak of this function determines if there is a charge-density wave instability, and at lower temperatures this peak becomes more pronounced, becoming singular only at zero temperature. As the carrier density increases this rises as the Fermi energy grows and eventually passes the temperature, establishing quantum coherence. However, the density of states also falls off as $n_{\rm el}$ increases, with $\chi(2k_F) \sim 1/n_{\rm el}$. Therefore, the potential emergence of a CDW phase clearly requires low temperatures and a high, but carefully tuned carrier density.

We ought to carry out a more systematic analysis with better estimates for parameters, but this is a decent starting point to guide the qualitative discussion. We now move to a related scenario, which involves the long-range Coulomb interaction rather than the phonon mediated interaction.

Stripe Crystal

It is reasonable to expect a form of Wigner crystal to be stabilized. In order to capitalize on both Coulomb repulsion and kinetic energy, a reasonable guess is a form of striped state where electron density occupies conducting chains but the filled chains space out so as to reduce Coulomb interaction. Consider a system where the wavefunction is given by ansatz consisting of a product state across different chains, and within each chain a Fermi surface. Let us consider each filled chain to be filled to Fermi level k_F such that each chain carries a linear charge density, guaranteed by Luttinger's theorem of

$$n_{\rm 1D} = k_F/\pi. \tag{18}$$

This leads to an average kinetic energy per particle of

$$\langle T\rangle = \frac{1}{n_{\rm 1D}}\int_{-k_F}^{k_F}\frac{dp}{2\pi}\frac{p^2}{2m} = \frac{1}{\pi n_{\rm 1D}}\frac{k_F^3}{6m} = \frac{E_F}{3}. \tag{19}$$

Now, let us consider the equal spaced chains with distance b between them. Then we consider an ansatz of every $\nu = 1, 2, ...$ chains being filled (so for $\nu = 1$ we have every chain filled, for $\nu = 2$ every other, so on), with the other chains being empty. This gives an overall two-dimensional charge density of

$$n_{\rm 2D} = n_{\rm 1D}/(\nu b) = \frac{k_F}{\nu\pi b}. \tag{20}$$

We now take the Coulomb repulsion into account. We use a rough model which only accounts for the repulsion between neighboring chains. We also use a model based on a point charge, and it is unclear at the moment how to generalize this to continuum distributions of lines of uniform charge. Nevertheless, we know the potential due to a linear distribution of charges when the charge is distance r away

$$V = -\frac{en_{1D}}{2\pi\epsilon_0}\log(r/b)$$

with a cutoff placed on the logarithm of order b, the lattice constant. The energy per unit area is

$$U = -\frac{e^2 n_{1D}}{2\pi\epsilon_0}\log(\nu)n_{2D}. \tag{21}$$

We combine the kinetic and potential energies to obtain an energy per electron of

$$E = \frac{\pi^2 n_{1D}^2}{6m} - \frac{e^2 n_{1D}}{2\pi\epsilon_0}\log(\nu). \tag{22}$$

We consider fixed areal charge density, implying

$$n_{1D} = \nu b n_{2D}. \tag{23}$$

This means that holding the total carrier density fixed while increasing the stripe separation requires increasing the charge per stripe. We find as a function of ν

$$E = \frac{\pi^2 b^2 n_{2D}^2}{6m}\nu^2 - \frac{e^2 b n_{2D}}{2\pi\epsilon_0}\nu\log(\nu) = \frac{\pi^2 b^2 n_{2D}^2}{6m}\left[\nu^2 - g\nu\log\nu\right] \tag{24}$$

where

$$g = \frac{3me^2}{\epsilon_0\pi^3 b n_{2D}} \tag{25}$$

is the tuning parameter, similar to a Wigner crystal. We find the ground state energy is minimized for $2\nu - g - g\log\nu = 0$. The solution to this equation exhibits a transition from $\nu = 1$ to $\nu = 2$ for roughly $g \sim 2$. At this point, the increased kinetic energy due to the increased Fermi level in the conducting chains is offset by the reduced Coulomb repulsion as the chains undergo a phase separation into stripes. Increasing g further we see a sequence of further separations into increasingly sparse chains. The condition of increasing g is affected by reducing the equilibrium carrier density, indicating this is essentially a Wigner crystallization, as argued in [3–5].

We comment that in this case, while the interchain direction remains frozen into a striped crystal, the intrachain dynamics remains coherent in this picture, being essentially regions of electron-rich liquids separated by empty insulating regions. Therefore transport along the chains is still coherent, barring effects due to disorder which is likely to dramatically reduce this transport. It is possible that for sufficiently strong interactions this will also exhibit an instability, e.g. of Peierls type into a checkerboard type insulator, but this probably requires substantial doping in order to obtain the finite density of states.

Clearly, this problem is very interesting and warrants more attention. In particular, it is important to develop a better model of the correlations and also account for the kinetic energy in the dispersive direction. More generally, we see that the "coupled" chain model suggested in [6] is extremely illuminating and if one can dope into this regime, it is likely that low-dimensional strongly-correlated physics will emerge.

* jpklein@mit.edu
† prineha@seas.harvard.edu
‡ loncar@seas.harvard.edu
§ fmross@mit.edu

[1] K. Hwangbo, Q. Zhang, Q. Jiang, Y. Wang, J. Fonseca, C. Wang, G. M. Diederich, D. R. Gamelin, D. Xiao, J.-H. Chu, et al., Nature Nanotechnology **16**, 655 (2021), URL https://doi.org/10.1038/s41565-021-00873-9.
[2] E. Ergeçen, B. Ilyas, D. Mao, H. C. Po, M. B. Yilmaz, J. Kim, J.-G. Park, T. Senthil, and N. Gedik, Nature Communications **13** (2022), URL https://doi.org/10.1038/s41467-021-27741-3.
[3] B. Spivak and S. Kivelson, Physical Review B **70**, 155114 (2004).
[4] V. Emery, E. Fradkin, S. Kivelson, and T. Lubensky, Physical Review Lett. **85**, 2160 (2000).
[5] H. Schulz, Physical Review Letters **71**, 1864 (1993).
[6] P. Wang, G. Yu, Y. H. Kwan, Y. Jia, S. Lei, S. Klemenz, F. A. Cevallos, R. Singha, T. Devakul, K. Watanabe, et al., arXiv (2021), arXiv:2109.04637.